# Crystallographic and Morphological Evidence of Solid–Solid Interfacial Energy Anisotropy in the Sn-Zn Eutectic System

SHANMUKHA KIRAN ARAMANDA, SUMEET KHANNA, SAI KIRAN SALAPAKA, KAMANIO CHATTOPADHYAY, and ABHIK CHOUDHURY

In this paper, we explore the morphological evolution during two-phase growth in the Sn-Zn eutectic system, which has a particularly low volume fraction of the minority Zn phase. The reason for this choice is its exotic nature, as even with such a low volume fraction, the reported morphology is ''broken-lamellar,'' in contrast to the usually expected hexagonal arrangement of Zn rods in the Sn matrix. Thus, the main objective of the study is to investigate the reasons behind this phenomenon. We begin by presenting experimental results detailing the morphology and crystallography of the eutectic microstructures under various combinations of thermal gradients and velocities in directional solidification conditions. Based on the crystallography and further specially designed experiments we find that the solid–solid interface between the Sn and Zn crystal is anisotropic. On the basis of the results, we propose a hypothesis that the presence of solid–solid interfacial energy anisotropy leads to the formation of predominantly broken-lamellar structures, even when the minority fraction is significantly low.

## I. INTRODUCTION

EUTECTIC solidification provides fascinating examples for complex pattern formation that have been studied experimentally and numerically.[1–14] If the solid–liquid interfaces of a eutectic system are non-faceted, then during steady-state solidification solid phases grow simultaneously and self-organize themselves into structures based on the dynamic balance between factors that influence solute diffusion and capillarity. The most commonly observed structures during binary eutectic growth are (i) lamellar/labyrinthine structure of two solid phases, (ii) rod structure of the minority phase in the matrix of the majority phase, and (iii) mixture of lamellar/labyrinth/rod morphologies. More complicated examples arise as the number of phases and components increase, and some recent studies on three-phase eutectic growth provide examples of complicated phase organization.[15–20]

One of the critical factors that influences morphological evolution during multi-phase growth is the volume fraction of the phases that result from the eutectic reaction. The volume percentages of the phases selected during growth are typically close to the value given by the mass balance between the far-field composition and the solid-phase compositions at the eutectic temperature. This is usually true for low solidification velocities (low Peclet number) but will show deviations at larger undercoolings due to appreciable changes in the solid compositions. The volume fractions of the phases that are dynamically selected as a result of the eutectic reaction are therefore in general dependent on the solidification conditions as well as the mobilities of the elements in multi-component systems. For two-phase growth in binary alloys, it is typically seen that for lower fractions of the minority phase, the rod morphologies are observed, while for close to equal volume fractions, a lamellar/labyrinthine morphology is commonly seen. Experimental evidence of the same is provided by Trivedi et al.[21] in the Al-Cu alloy where different microstructures with the change in the far-field compositions are achieved that consist of the rod, lamellar, and mixed growth forms. While energetic arguments by Cooksey et al.[22] and others lead to critical values of the volume percentages demarcating the regions of stability of the rod and the lamellar morphologies, this has not been experimentally verified, and examples to the contrary are available, particularly from dynamical

SHANMUKHA KIRAN ARAMANDA, SUMEET KHANNA, SAI KIRAN SALAPAKA, KAMANIO CHATTOPADHYAY, and ABHIK CHOUDHURY are with the Department of Materials Engineering, Indian Institute of Science, Bangalore 560012, India. Contact e-mail: abhiknc@iisc.ac.in

phase-field simulations. Simulation studies by Plapp et al.[23] and Gránásy et al.[24] show that there is no clear, distinct volume fraction where the rod-lamellar transition occurs, and there are liquid compositions (which influence the volume fractions) where mixed morphologies may be observed. Moreover, the rod-lamellar transition is shown to be dependent on the history of the solidification process,[23] and thereby, there is no pattern selection in the strong sense as a function of change in the volume fraction of the phases. While the influence of volume fractions on morphological evolution is fairly well understood during two-phase growth in binary alloys for isotropic situations, several examples to the contrary are available wherein, even for significantly low volume fractions of the minority phase the morphology is biased towards a lamellar structure in contrast to a rod microstructure. Some of the examples where lamellar (i.e., broken-lamellar) morphology is observed even when the volume percent of the minority phase is less than 10 pct are Ag-Bi,[25–30] Ag-Pb,[29,31] Ag-Sn,[32,33] Al-Au,[34] Al-Sb,[35] Al-Sn,[6,31] Bi-Mg,[6] Bi-Mn,[36] Bi-Zn,[27,30] Cd-Ge,[37] In-Zn,[31,38] Sn-Zn,[3,39–45] and some organic systems.[46] One of the key factors that can lead to the stabilization of the lamellar structure over the rod morphology is the presence of anisotropy in the solid–solid interfacial energy, which is hinted at in Reference [47], while experimental results illustrating the possible influence of solid–solid interfacial energy anisotropy are provided by Chadwick,[3] Jaffrey, and Chadwick[40] along with Caroli and co-authors.[48] In recent years the study of anisotropic eutectics has lead to new observations and inferences about the influence of solid–solid interfacial energy anisotropy. In a review paper,[14] the authors postulate that anisotropy in the solid–solid interphases would favor the formation of lamellae over rods. Studies in thin-film growth experiments have resulted in new findings that the presence of strong anisotropy in the solid–solid interfacial energy can lead to locking of the orientations of solid–solid interface with respect to the growth direction.[48–53] The studies[50–53] are particularly interesting as the authors propose a new method of determining the strength of anisotropy by determining the trace of the solid–solid interface using a rotating directional solidification (RDS) setup and thereby the authors provide evidence for the presence of anisotropy in the solid–solid interfacial energy while also illustrating the influence of anisotropy on the morphological evolution. More recently, it has also been shown that such anisotropy can lead to well-aligned lamellar morphologies in contrast to labyrinthine growth forms during bulk solidification using dynamical phase-field simulations[54] as well as in experiments.[55] Similarly, experimental studies by Bottin-Rousseau et al.[56] have shown that coincident low-index lattice planes between the solid phases can lead to special orientations with lower interfacial energies leading to locked lamellar eutectic growth in thin films of (In)-In$_2$Bi binary system. Finally, Mohaghegh et al.[57] have studied the effects of interphase boundary anisotropy on the three-phase growth dynamics in β-(In)-In$_2$Bi-γ-(Sn) ternary eutectic system. Therefore, there is enough evidence to show that the presence of anisotropy in the solid–solid interfacial energy can influence the morphological evolution during multi-phase eutectic growth. However, there is still a lack of understanding with regard to the influence of the solid–solid interfacial free energy anisotropy on the rod-to-lamellar (or vice-versa) transitions in eutectics.

This drives us to the main objective of the paper which is to understand the formation of a broken-lamellar structure in contrast to the rod morphology during solidification of the Sn-Zn eutectic alloy that has a minority phase percent of 9 pct of the Zn-rich phase. The reason for choosing this system is that none of the previous studies[6,39–45,58–60] on this system conclusively establish the reason behind the formation of the broken-lamellar morphology. Further, we would like to clarify the existence of crystallographic orientation relationships, given that no unique relationships were observed in earlier studies.[40,41,61–64] We postulate based on the past experimental observations as well as our own that the principal reason behind the formation of this broken-lamellar morphology in contrast to rods is the presence of anisotropy in the solid–solid interfacial free energy.

Following is a brief structure of the paper. We begin with the description of the directional solidification setup in Section II. Thereafter, we elaborate on the morphological and crystallographic characterization of the directionally solidified samples in Section III. Using the results obtained from characterization tools, we analyze the reasons behind the biasing towards a broken-lamellar microstructure.

## II. EXPERIMENTAL DETAILS

### A. Alloy Preparation

Eutectic alloys were prepared based on the composition (i.e., Sn-8.8 wt pct Zn) given in the phase diagram as reported in Reference [64]. High-purity 99.99 + pct (Alfa Aesar) elements were used for making the alloys. Synthesized alloys were filled in quartz tubes (4 mm inner diameter, 6 mm outer diameter) and sealed after creating low pressure ($10^{-5}$ mbar) inside the tubes using rotary/diffusion pumps. These alloys, which are sealed in quartz tubes, are used for directional solidification experiments.

### B. Directional Solidification Apparatus

We have used a modified Bridgman-type apparatus (see Figure 1(a)) for conducting directional solidification experiments. The setup contains three zones to enhance the control of heat transfer during solidification. The essential features of the setup are an isothermal hot zone and an isothermal chill zone which are separated by a thin ceramic-based insulation zone constituting the adiabatic zone. The hot zone is obtained using resistance heating (Kanthal-A is heating element), whereas the chill zone has a continuous circulation of constant temperature water through a copper chill. Hollow
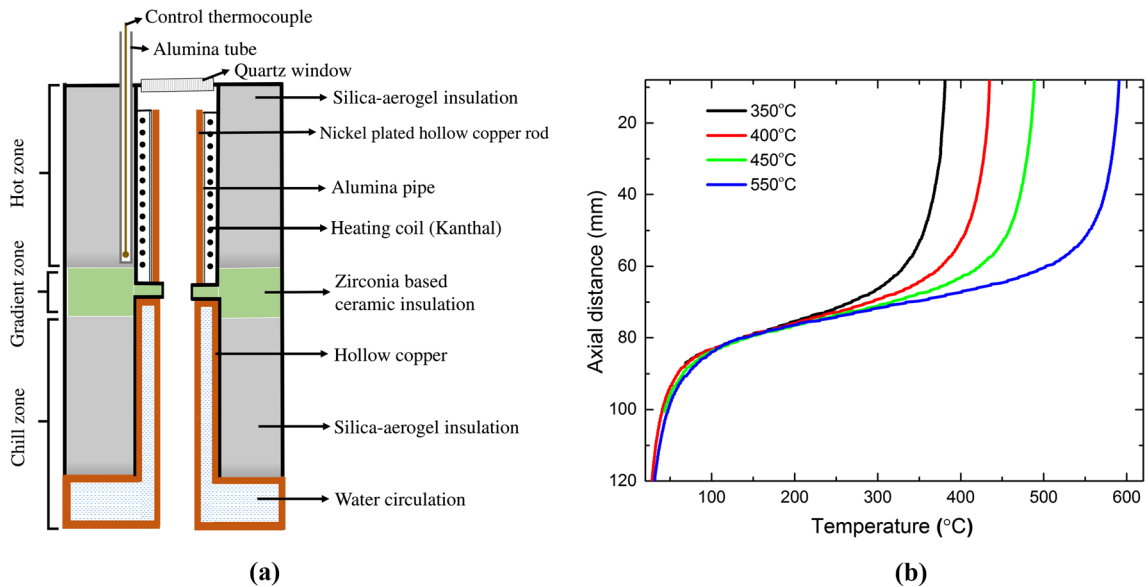
Fig. 1—Schematic of the modified Bridgman apparatus is shown in (a), while plots in (b) display the axial temperature distribution with distance from the hot zone, for different temperatures of the hot zone; where the origin of distance axis is at the center of the hot zone and the distance is measured until the center of the chill zone. Please note that the schematic in (a) is not to the same scale as in (b). Axial lengths of the hot zone, gradient zone, and chill zone are 100, 10, and 80 mm respectively, while the inner diameters are 20 mm for hot and chill zones, whereas gradient zone has 18 mm inner diameter.
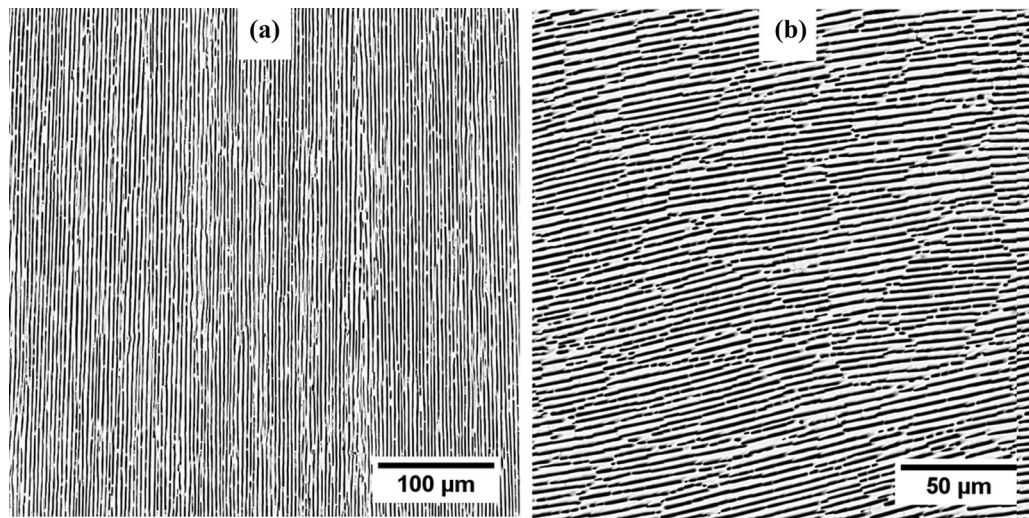


Fig. 2—Scanning electron micrographs obtained using backscatter electrons (BSE) after etching the alloy solidified at 2.5 μm/s and imposed temperature gradients of 14.5 °C/mm, where (a) is the longitudinal section (growth direction is from bottom to top), while (b) is the transverse section, growth direction is towards the reader.

copper rods placed concentrically with the heating elements are used to obtain a uniform distribution of temperature in the hot zone and heat transfer right up to the adiabatic zone. The purpose of the insulation zone in between is to reduce the heat transfer between the hot and chill zones and thereby automatically result in the establishment of a gradient between the hot and cold zones. In order to maintain a stable solidification front without any mechanical vibrations, the entire furnace assembly is moved relative to the stationary sample, which is initially kept in the hot zone. The sample is moved from the hot zone to the chill zone with the imposed directional solidification conditions (fixed temperature gradient and fixed velocity), where the required solidification velocity is imposed using a gearbox and a stepper motor that translates the furnace along a fixed linear drive. The axial temperature in the setup was measured using a thermocouple that is held stationary while the furnace is made to traverse a given length. This delivers the temperature distribution with distance along the furnace that is plotted in Figure 1(b) for different set temperatures of the hot zone. We measured the
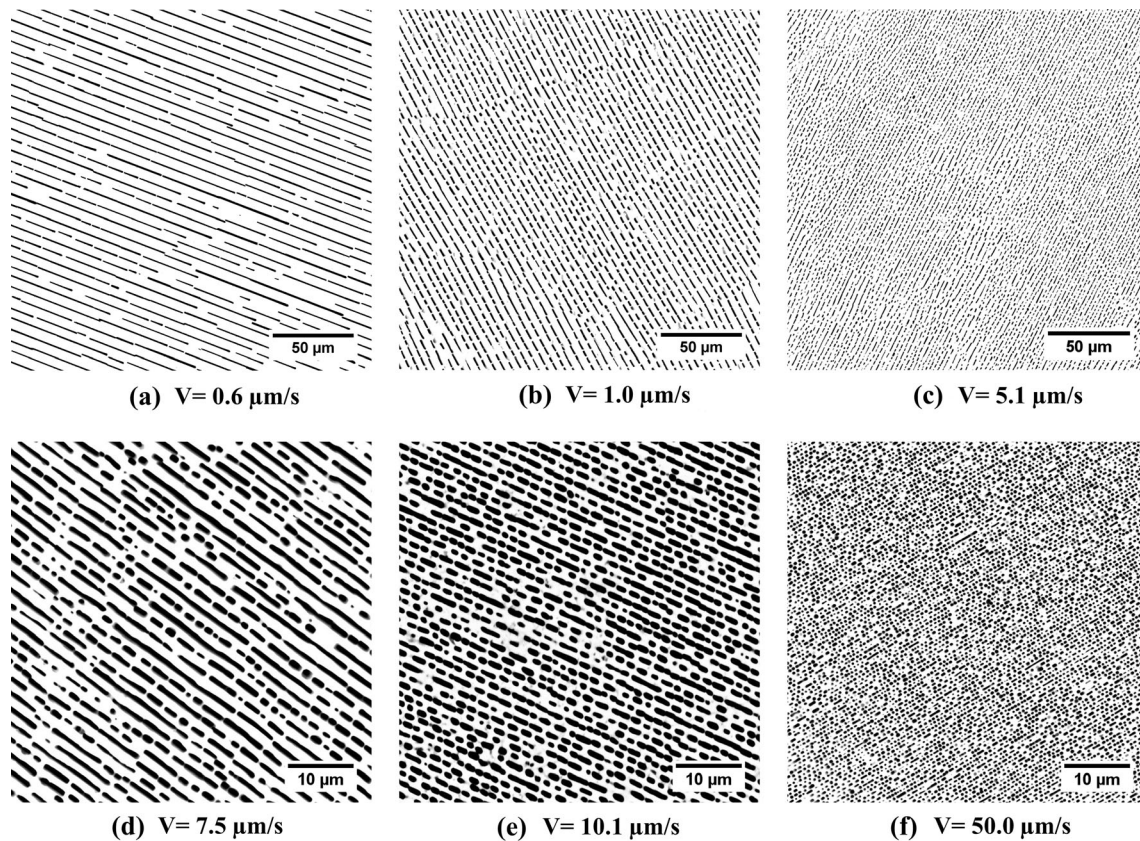
Fig. 3—Transverse section SEM images of directionally solidified Sn-Zn eutectic alloy at different velocities, *i.e.,* (*a*) through (*f*) correspond to 0.6, 1.0, 5.1, 7.5, 10.1, 50.0 $\mu$m/s, respectively. Images are captured in BSE mode after etching the samples.
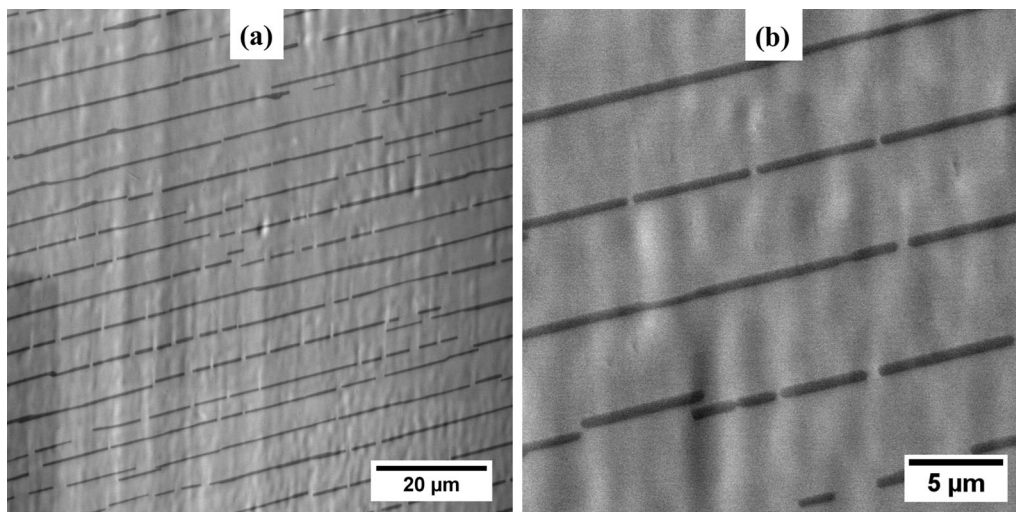


Fig. 4—Transverse section images of the unetched Sn-Zn alloy solidified at 0.6 $\mu$m/s, low-magnification image in (*a*) and high-magnification image in (*b*), where bright part is Sn-rich phase and dark part is Zn-rich phase. Images are captured using backscatter electrons, subsequent to fine ion-milling.

temperature gradients at the melting temperature of the alloy from the temperature profiles obtained that are derived once the steady-state thermal equilibrium is achieved. This temperature distribution in the absence of the sample is essentially the imposed temperature gradient in the furnace and differs from the value at the liquid–solid interface, since the temperature distribution inside the quartz tube containing the sample involves additional heat transfer through the solid and the liquid. We computed the temperature profiles at the solid–liquid interface through a heat-transfer model capturing all the essential modes of heat transfer and using the partial
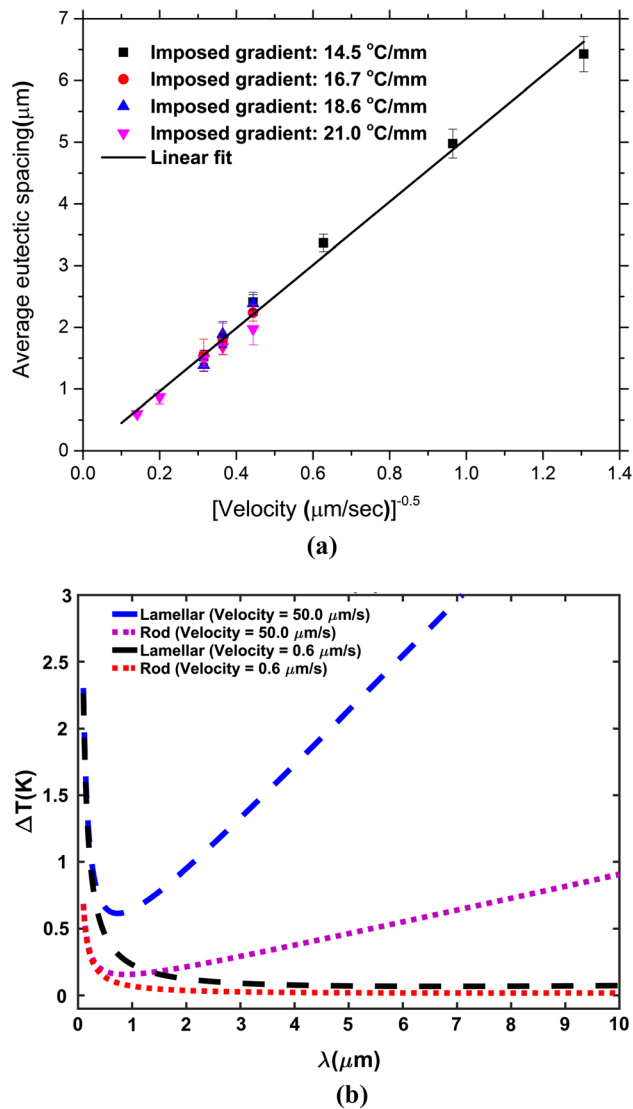
**(a)**



**(b)**

Fig. 5—(a) Variation of average spacing with velocity and (b) average undercooling with eutectic spacing.

differential equation manipulation library in Open-FOAM[65] that allow us to precisely ascertain the thermal gradients at the solidification interface, the details of which are mentioned in the Appendix A. Using this furnace, we directionally solidified the eutectic alloy up to 80 mm in length (4 mm in diameter) at different imposed temperature gradients (14.5, 16.7 18.6, 21 °C/mm ) and different pull velocities ($V$ = 0.6, 1.1, 5.1, 7.5, 10.1, 50.0 $\mu$m/s).

### C. Metallographic Examination and Spacing Measurements

We sectioned the directionally solidified samples at equally spaced intervals along the growth direction using a wire electrical discharge machine (WEDM) in transverse and longitudinal directions. Thereafter we cold mounted using epoxy resin and then polished the samples for imaging. For etching the samples, we utilized a solution of 80 pct glycerol, 10 pct nitric acid,

and 10 pct acetic acid which leads to pitting of the Zn-rich regions in the samples that are consequently used for Scanning Electron Microscope (SEM) (FEI make, model: Quanta 400 ESEM) imaging. The eutectic spacings are obtained by performing FFT (Fast Fourier Transform) of the SEM images of the transverse sections. We average the spacing obtained over 8-10 images spanning different regions of transverse sections cut at 40, 50 mm distance from the start that is around the middle of the sample where the spacing variation is small and is representative of growth according to the imposed conditions. This procedure is essential as both in the early part of the solidification as well as in the end, the thermal and solutal conditions are transient in nature and therefore need to be omitted from the analysis. The field of view for measurement is chosen such that it contains maximum number of resolved lamellae, *i.e.*, 400 × 400 $\mu$m$^2$ for 0.6, 1.1 $\mu$m/s samples, 200 × 200 $\mu$m$^2$ for 5.1, 7.5, 10.1 $\mu$m/s samples, 100 × 100 $\mu$m$^2$ for 50.0 $\mu$m/s samples. Additionally, in order to avoid mechanical and chemical polishing artifacts (Sn-rich phase is a mechanically very soft phase, and Zn-rich phase is a chemically very active phase), we have employed a separate method of sample preparation for electron backscatter diffraction (EBSD) analysis, in which, we have utilized the dual-beam platform (FEI Helios G4) for final polishing through precision ion beam milling using gallium ions at grazing incidence angle close to zero and subsequently performed EBSD in the same instrument. The precision ion beam milling method is also used in sample preparation prior to the imaging of unetched specimens shown in the paper. EBSD scans are performed at an accelerating voltage of 25kV with a step size of 60.0 nm for samples solidified at 0.6, 1.1, 5.1, 7.5, 10.1 $\mu$m/s and 20.0 nm for sample solidified at 50 $\mu$m/s. Data obtained from EBSD scan are directly used without any cleanup, however, data points having confidence index (CI) value greater than 0.1 are only selected for plotting and analysis.

## III. RESULTS AND DISCUSSIONS

### A. Morphology Aspects

Figure 2 depicts the microstructure ((a) shows the longitudinal section, (b) shows the transverse section) of the Sn-Zn alloy obtained from the directionally solidified sample at an imposed velocity of 2.5 $\mu$m/s and imposed temperature gradient of 14.5 °C/mm. The longitudinal section highlights the alignment of the eutectic phases along the direction of the temperature gradient, while the transverse section shows the "broken" lamellar morphology of the Zn-rich phase. As has been mentioned in the previous sections, this is a surprising result, given the small volume fraction of the Zn-rich phase. Further, this structure is quite different from that of the irregular growth structures of eutectic phases.[66] Our observations match with previous studies[39–45] on this alloy. Figure 3 shows the range of eutectic microstructures of the alloy solidified
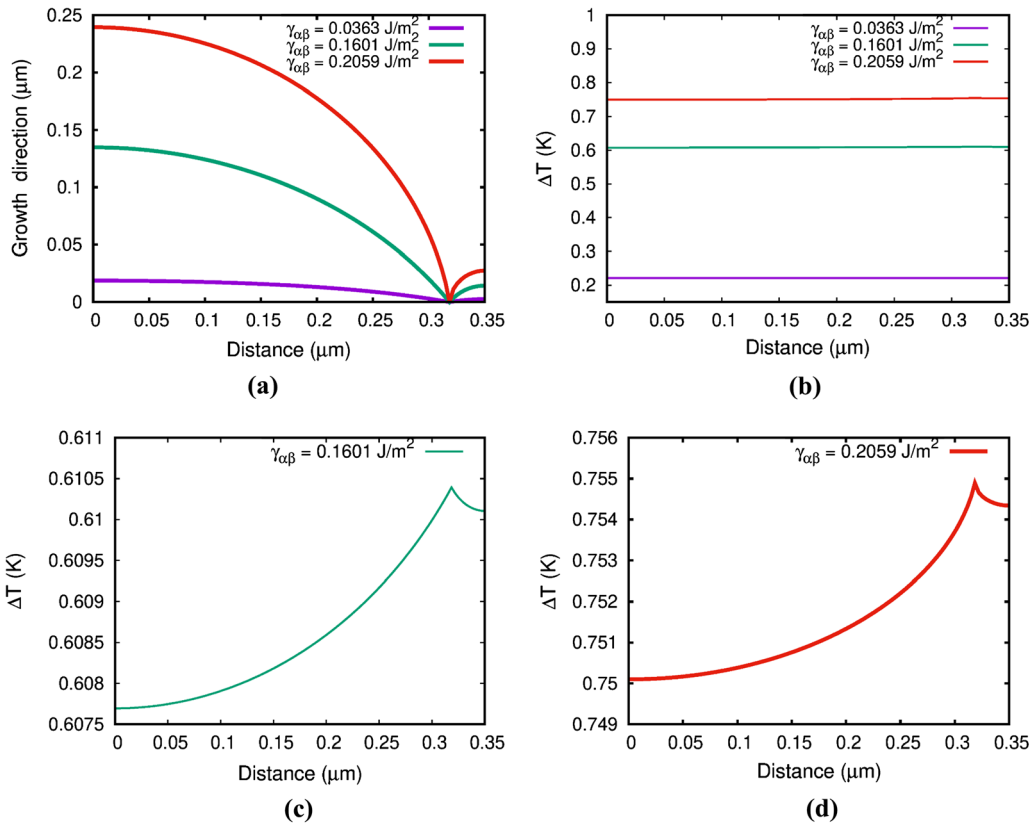
Fig. 6—(*a*) Interface shape calculated for different values of the solid–solid interfacial energy, (*b*) displays the corresponding undercooling for the different choices of the solid–solid interfacial energy, while (*c*) and (*d*) show enlarged views of the variation of the undercooling across the solid–liquid interface for particular values of the solid–solid interfacial energy.

at different velocities ($V$ = 0.6, 1.0, 5.1, 7.5, 10.1, 50.0 $\mu$m/s). Globally, at all velocities, the transverse section images show the evidence of a broken-lamellar type of arrangement of the Zn-rich phase. Connections of broken-lamellar fragments leading to increase in average lamellar fragment length become more with the decrease in velocity, however, the influence of the imposed thermal gradients on connections is minor.

Because the previous SEM images are obtained post etching, which alters the volume fraction of the phases, we utilize the dual-beam microscope (FEI Helios G4) for imaging subsequent to polishing of the surface with ion beam. This retains the information about the spatial distribution of the Zn-rich phases as well as their volume fractions post solidification. High-resolution images captured for the sample solidified at 0.6 $\mu$m/s shown in Figure 4, depict the actual distribution of both the phases and the phase fraction, whereas in the etched samples the phase fraction of Zn appears to be higher than actual due to the extent of the pitting reaction that invades the Sn matrix. Consequently, we have utilized EBSD data for phase quantification and the derived phase fractions are close to that expected at the eutectic liquid composition (refer supplementary material, Velocity = 0.6 $\mu$m/s, Figure S1). This confirms that indeed, the liquid composition is at the eutectic during solidification and additionally, the fact that the

morphology of the Zn-rich phases appears lamellar in the SEM images is not due to etching of the samples.

The lamellar spacing that is the principal length scale in the microstructure is not altered with etching as the centroids of the phases remain unchanged. Therefore, we have utilized the SEM images post etching and evaluated the average spacings using FFT, for each of the thermal gradients and the velocities and the results are shown in Figure 5(a) where error bars correspond to the standard deviation of the data obtained over several images. We linearly fit the observed spacings $\lambda$ against $V^{-0.5}$ ($V$ is the velocity), that is also highlighted in Figure 5(a), where the slope of the linear fit directly reveals the scaling constant $\lambda^2 V$ that is approximately 27.04 $\mu$m$^3$/s for the Sn-Zn alloy at the eutectic composition.

If we assume that our observed morphology is close to a lamellar for most of the imposed conditions, then the corresponding undercooling *vs.* spacing relation can be calculated using the value of $\lambda^2 V$ obtained from the experiments. Similarly, we calculated the undercooling *vs.* spacing relationship for the rod morphology of the alloy (refer Appendix B for this calculation). The undercooling *vs.* spacing relations for both the rod and the lamellae morphologies are plotted for the 50.0 $\mu$m/s and the 0.6 $\mu$m/s velocities in Figure 5(b). For both velocities, we see that the minimum undercooling for the rod is lower than that of the lamellae, which would
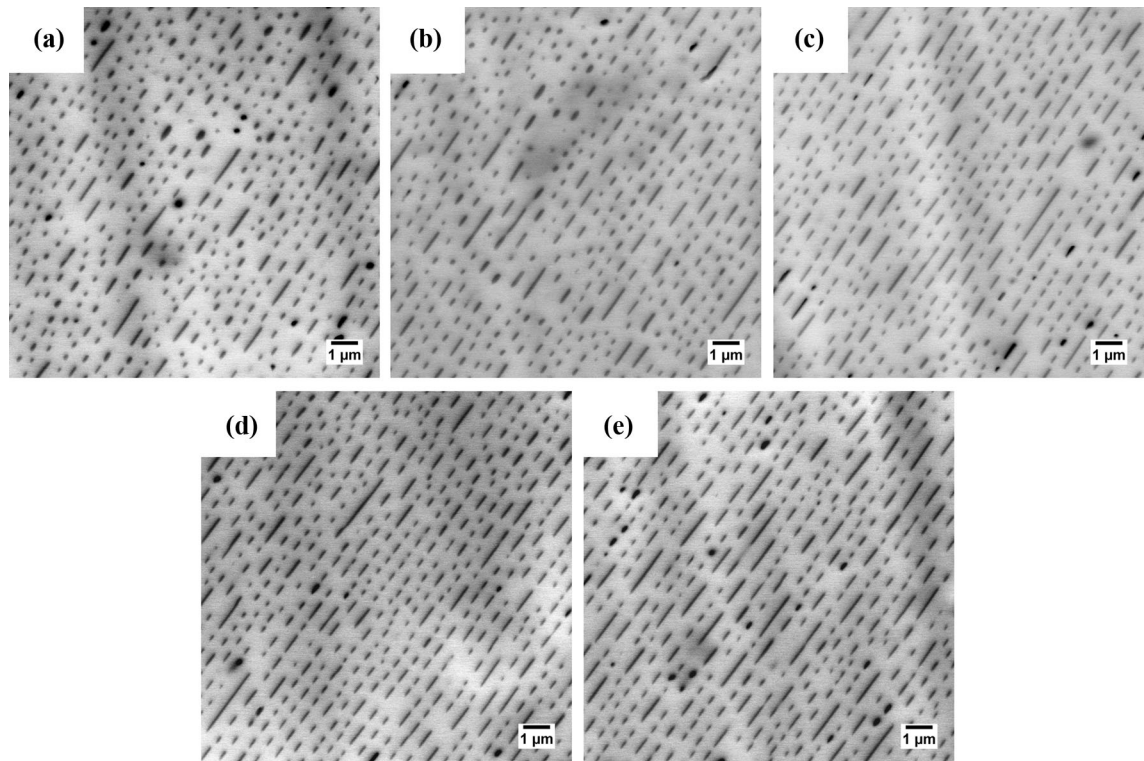
Fig. 7—Images captured using a SEM, which are taken at equally spaced transverse sections along the growth direction, following the same eutectic grain of the sample solidified at 50 $\mu$m/s. (a) is 20 mm from the bottom, (b) is 30 mm from the bottom, (c) is 40 mm from the bottom, (d) is 50 mm from the bottom, (e) is 60 mm from the bottom.
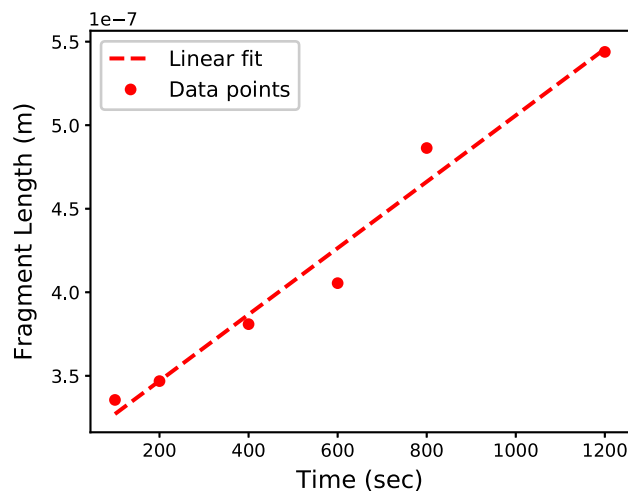


Fig. 8—Variation of average length of lamellar fragment with time of solidification.

suggest going by the arguments in the Jackson–Hunt paper[47] that the rod would be the preferred microstructure. However, this seems contrary to our experimental observations which seem to suggest that the morphologies are biased more towards lamellae than rods. A possible explanation is already provided by Jackson and Hunt[47] where they propose that anisotropy in the solid–solid interfacial energy may lead to the lamellar morphology possessing a minimum undercooling that is

lower than that of the rod microstructure. This is because, for a lamellar morphology, the alignment of the lamellae such that the solid–solid interfaces correspond to the minimum interfacial energy orientations would lead to a much lower undercooling than the corresponding case of the rod morphology where the solid–solid interface possesses a larger proportion of orientations that are of higher solid–solid interfacial energy leading to increased undercooling at the growth front.

We have computed the interface shapes of the lamellar morphology growing at 50.0 $\mu$m/s for varying magnitudes of the solid–solid interfacial energy and, as a consequence, also computed the undercooling of the solid–liquid interfaces, Figure 6 (the details of the computation procedure are provided in the Appendix C). Different values of $\gamma_{\alpha\beta}$ are obtained by varying the angle $\theta_{\alpha l}$ ($\sin\theta_{\alpha l}$) and using constant $\gamma_{\alpha l}$ for both the phases (determined by taking the Gibbs–Thomson coefficient[43] of $\alpha$-liquid and entropy of fusion derived from thermodynamic database[67]). As depicted in Figure 6(b), we see that the solid–liquid interfacial undercooling decreases with reduction in the solid–solid interfacial energy. This variation of the interfacial undercooling can be attributed to the contribution from the curvature undercooling which gets modified upon changing the solid–solid interfacial energies. Extrapolating to the case of a 3D growth front, in the presence of solid–solid interfacial energy anisotropy, one expects the undercooling along the triple-line to vary, wherein
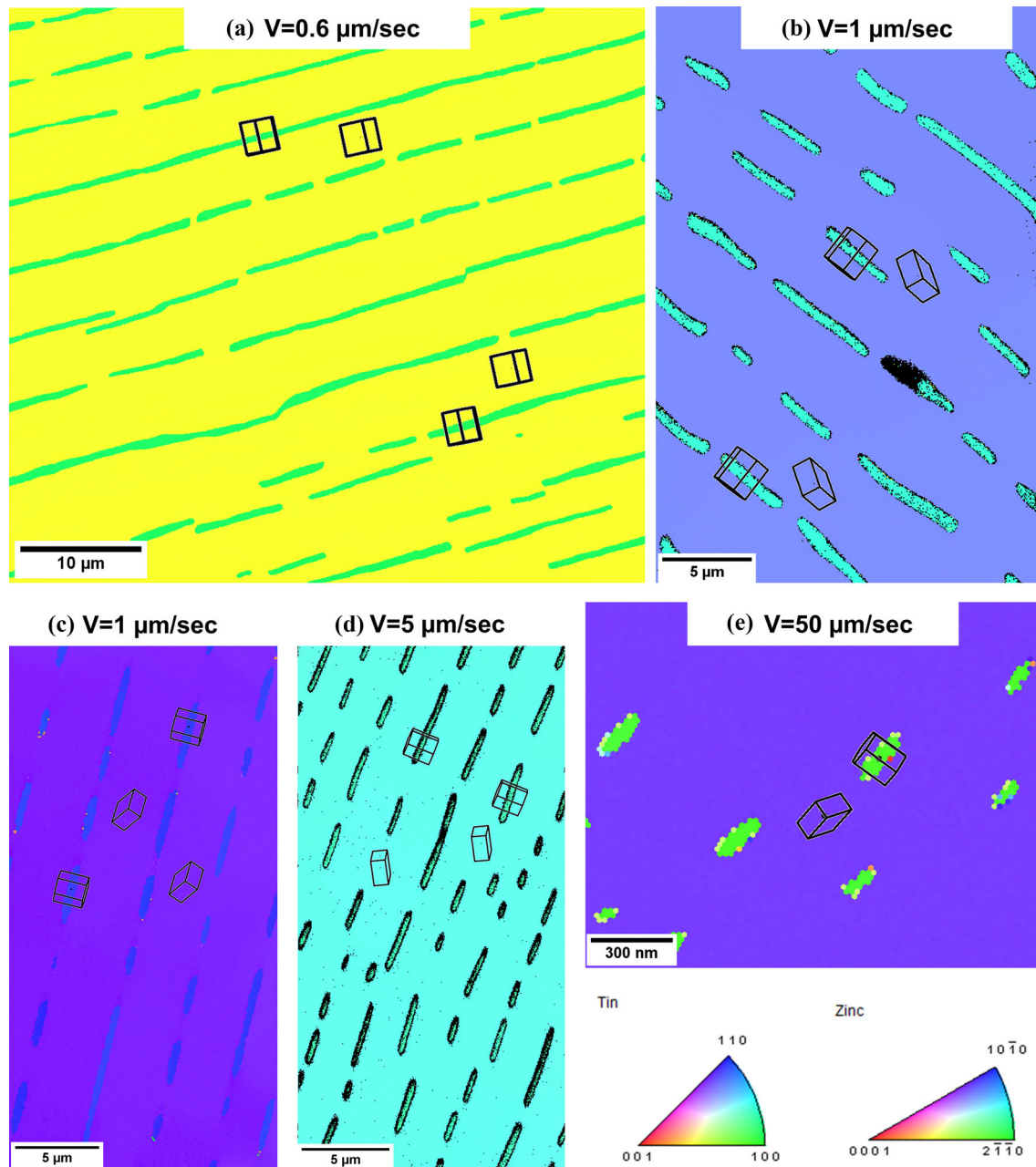
Fig. 9—Inverse pole figure maps of the alloy taken from different samples, where (*a*) through (*e*) are from the samples solidified at 0.6, 1, 1, 5, 50 $\mu$m/s, respectively. The orientation of the unit cells is depicted in each of the phases that reveal that the basal plane of Zn is always parallel to the lamellar interface (given that this transverse section is a true section, *i.e.*, the lamellae plates are oriented exactly perpendicular to the plane of the paper).

orientations for which the solid–solid interfacial energy is larger will also be regions where the solid–liquid interfacial undercooling is greater. In this configuration, a microstructural evolution process that leads to the merging of broken-lamellar/rod fragments such that the higher undercooling regions of the solid–liquid interfaces are eliminated, will result in a lowering of the average solid–liquid interfacial undercooling. Additionally, it would result in a natural biasing of the microstructure that would closely resemble the merging of lamellar fragments along well-defined directions leading to the appearance of a periodic arrangement of broken-lamellae. We find experimental evidence of this in our SEM images as seen in Figure 7, where we see the gradual alignment of lamellae along a well-defined direction and consequently increase in the average length of the broken-lamellar fragment with time, which is shown in Figure 8.

(a1) Pole figures of Sn

(a2) Pole figures of Sn

(b1) Pole figures of Zn

(b2) Pole figures of Zn

Velocity: 0.6μm/sec

Velocity:1.0μm/sec

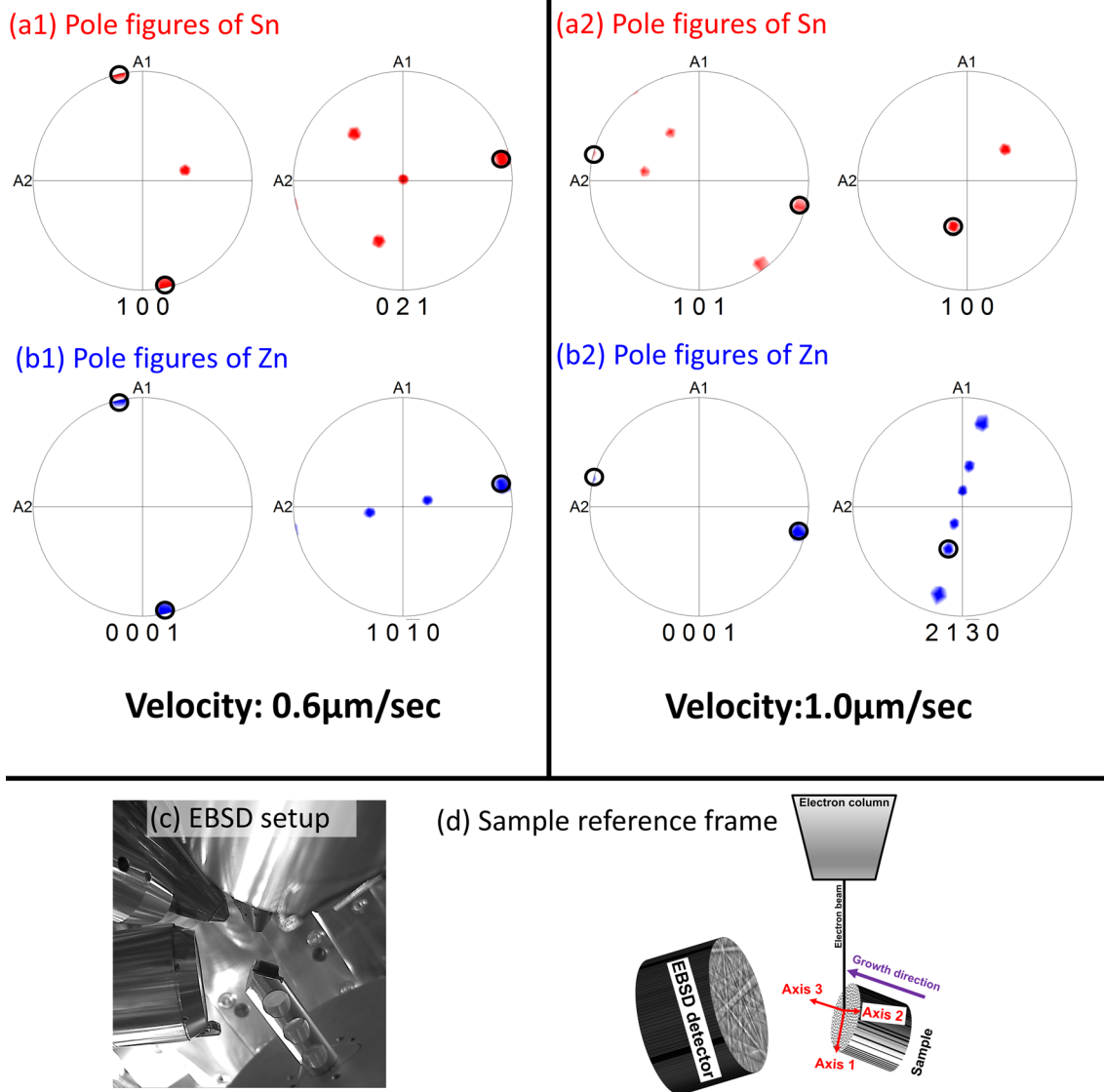(c) EBSD setup

(d) Sample reference frame

Fig. 10—The two orientation relationships that we derive from our experiments at different velocities are depicted in ((a1)(Sn), (b1)(Zn)) and ((a2)(Sn), (b2)(Zn)) pole figure sets, respectively. Pole figures ((a1)(Sn), (b1)(Zn)) corresponding to 0.6 μm/s, reveal the OR as one of the poles in Sn{100} family || Zn{0001} and one of the poles in Sn{021} family || one of the poles in Zn{01$\bar{1}$0} family, while ((a2)(Sn), (b2)(Zn)) corresponding to 1.0 μm/s, show that one of the poles in Sn{101} family || Zn{0001} and one of the poles in Sn{100} family || one of the poles in Zn{21$\bar{3}$0} family. (c), (d) show the sample setup and reference frame in EBSD, respectively.

## B. Crystallographic Orientation Aspects

During solidification of the eutectic, the Sn-rich phase crystallizes as the tetragonal A5 structure whose space group is I4$_1$/amd (typically called as body-centered tetragonal, BCT), and the Zn-rich phase crystallizes as the hexagonal A3 structure whose space group is P6$_3$/mmc (traditionally called as hexagonal close packed, HCP).[64] We find crystallographic orientation relationships corresponding to the (Sn) and the (Zn) phases that are reported in the literature.[40,41,61–64] However, we do not find a unique relation being reported among the findings from these studies. Chadwick et al.[40,63] report an orientation relation that suggests that the {$\bar{1}$01} planes of Sn are parallel to {$\bar{1}$012} planes of Zn while the

⟨120⟩ directions of Sn are parallel to ⟨01$\bar{1}$0⟩ directions of Zn in all of their experiments (irrespective of rod/lamellar morphology). This relation is, however, contradictory to the relations reported by Straumanis et al.[61] that are referred to in a separate work[63,64] who find that the {100} planes of Sn are parallel to {0001} planes of Zn and ⟨001⟩ directions of Sn are parallel to ⟨01$\bar{1}$0⟩ directions of Zn. The differences could be due to the technique that the authors employ in order to obtain the orientation relation, wherein, Chadwick et al.[63] have used conventional X-ray texture diffractometry, whereas Straumanis et al. have obtained the relations based on Laue X-ray reflection method.[64] The problem with these techniques is that X-ray diffraction is not a very sensitive tool for determining crystal orientation relations. In order to clarify the presence/absence
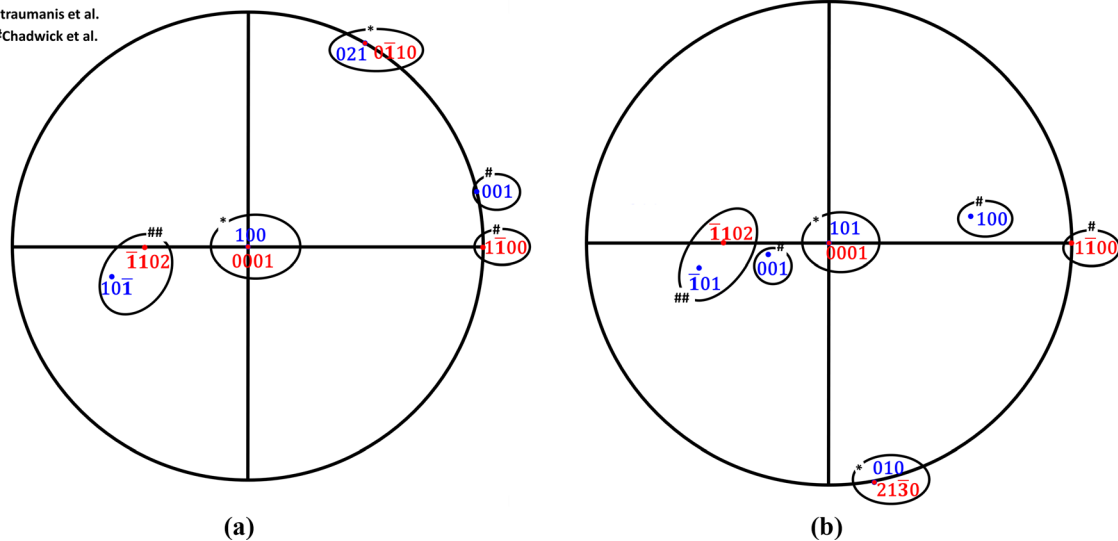
Fig. 11—(a) Superimposed stereographic projection obtained upon matching the basal planes {0001} of Zn with {100} of Sn, and rotating around these normal vectors to match the second set of planes (0$\bar{1}$10) of Zn with (021) of Sn. (b) Superimposed stereographic projection obtained upon matching the basal planes {0001} of Zn with (101) of Sn, and rotating around these normal vectors to match the second set of planes (21$\bar{3}$0) of Zn with (010) of Sn. This sets the orientation of the unit cells/crystals.

of a crystallographic orientation relationship, we have utilized a more sophisticated tool EBSD which provides local information, that is currently available. The Kikuchi patterns which are used for determining the crystallographic orientation in EBSD are extremely sensitive to crystal orientation[68,69] and thereby are more reliable for determining the orientation relationships. EBSD is performed on the transverse sections of the solidified samples. The patterns obtained from EBSD in all samples have an average confidence index more than 0.3 which can be taken as a very accurate measurement.[70] The results obtained from the EBSD are shown in the form of inverse pole figure maps (Figure 9) (Refer supplementary information file for pole figures and deduced orientation relationships). We will first mention the principal finding in our paper, which is that the basal planes of Zn are always parallel to the solid–solid interfaces in the lamellar plate morphology. This points towards the possibility that this is a low-energy orientation for the solid–solid interface and any other orientation is probably energetically unfavorable (detailed description follows). Secondly, we have observed predominantly two orientation relations in our experiments, i.e., first OR is one of the poles in Sn{100} family || Zn{0001} and one of the poles in Sn{021} family || one of the poles in Zn{0$\bar{1}$10} family; and the other OR is one of the poles in Sn{101} family || Zn{0001} and one of the poles in Sn{100} family || one of the poles in Zn{21$\bar{3}$0} family, which are depicted in Figure 10 (These are obtained by comparing the pole locations of each phase with respect to the sample reference frame, refer supplementary information file for data from experiments performed at different velocities). We note that ORs may also be determined using Kikuchi patterns obtained from a Transmission Electron Microscope (TEM), although, the effort required

for the sample preparation for EBSD is much less compared to that in TEM. However, validation of the observed ORs using TEM remains as a scope for future work. We have chosen to report the OR using parallel plane normal vectors in both crystals, which should be geometrically equivalent to the more frequently used method of a combination of plane and a direction, where the direction is in the plane. The combination of planes in each crystal are chosen such that these are perpendicular to each other (one is in the center and other is in the great circle of the stereographic projection, see Figures 11(a) and (b)). We have verified geometrically by comparing the resultant orientations of the unit cells that would result with each of the OR mentioned in the previous citations. We find that these are indeed different and are highlighted in the stereographic projections plotted for our results, as shown in Figure 11. For instance, the OR from Straumanis et al.[61] has one set of parallel planes, the same as in one of our OR, i.e., ({100} of Sn || {0001} of Zn). The set of directions from Straumanis et al.[61] that are indexed as [h,k,i,0] are also the normal vectors of the planes with the same {h,k,i,0} and therefore, we have plotted the poles of the normal vectors of the planes corresponding to the index of the parallel directions. This is highlighted as in Figure 11(a) where we do not find a match between the said directions {001} of (Sn) and {0$\bar{1}$10} of (Zn) that are encircled. Therefore, the resultant orientation of the crystals with respect to each other is different between what is reported by Straumanis et al.[61] and what we find in our work. Further, the relations reported by Chadwick et al.[63] are entirely different from that of our results. This is highlighted in Figure 11(a), where the poles corresponding to the suggested parallel planes by Chadwick et al.[63] clearly do not superimpose when we impose the OR that we find in our work as the
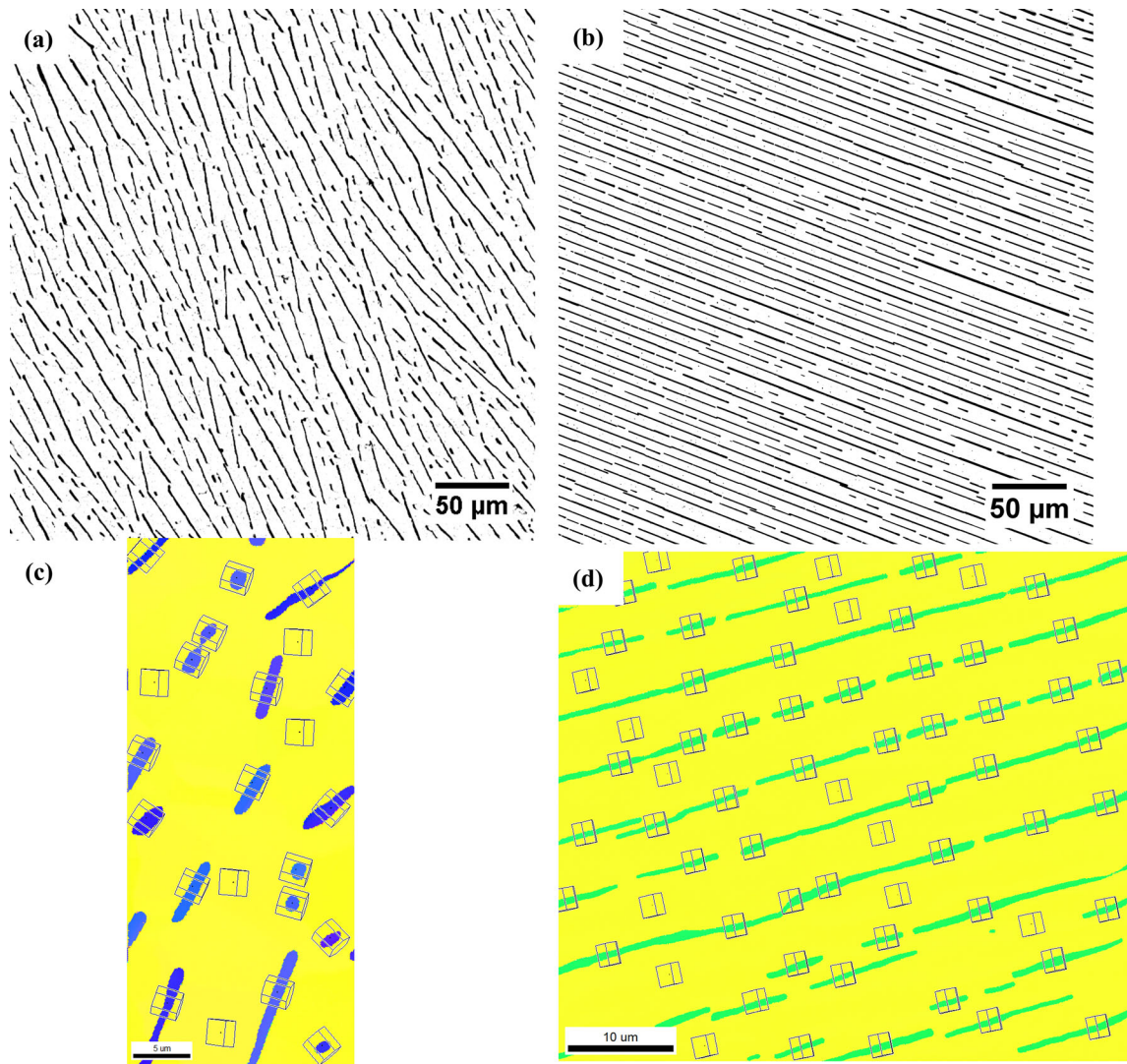
Fig. 12—Comparison of the SEM images during the initial transient in (*a*) and later during the solidification in (*b*). The inverse pole figures in (*c*) corresponding to the SEM image in (a) reveals the presence of multiple variants of Zn growing along with Sn, while later during the solidification a single orientation of Zn survives as highlighted in (*d*). The solidification is carried out at 0.6 $\mu$m/s.

crystallographic relation between the Sn and Zn crystals. The mismatch with the ORs is also true for the second orientation relation that we find in our work as shown in Figure 11(b). While our relations are therefore different from that reported in the literature, however, we do not claim that this is an exhaustive set and there could be other possibilities that might have nucleated but are outgrown by crystals with different orientations. Here, we concur with the findings of Jaffrey and Chadwick[40] that it is possibly Sn that nucleates first followed by Zn. Our hypothesis is that among the orientations of Zn that form, the ones that lead to a lower interfacial energy along with a favorable growth direction with respect to the imposed thermal gradient survive and are the ones that are observed at the end of the directional solidification experiment. This fact can be appreciated by comparing the SEM and EBSD images during the initial transient and those occurring later during the solidification (refer Figure 12). Here, we see that while multiple variants of Zn grow along with Sn during the

initial transient, selection of a single variant occurs as solidification progresses that is highlighted in the inverse pole figure of the microstructure occurring later during solidification.

The basal planes of (Zn), as well as the (100) and (101) planes of (Sn), are the closest packed planes in comparison to the other planes, and this might lead to the formation of a low-energy solid–solid interface between the (Sn) and (Zn) crystals. The growth competition among the variants that might nucleate must undoubtedly depend on the solid–solid interfacial energy, and this is certainly an interesting topic for future research. However, the common thing we find in all our experiments is that the basal planes {0001} of (Zn) and either one of the planes in {100} or {101} family of (Sn) are always parallel to the lamellar interface. The results reported by Straumanis et al.[61] also have the (Zn) basal planes and (100) planes of (Sn) parallel to the lamellar interface.[63] This type of observation is not just limited to the Sn-Zn system, the Bi-Zn eutectic system which
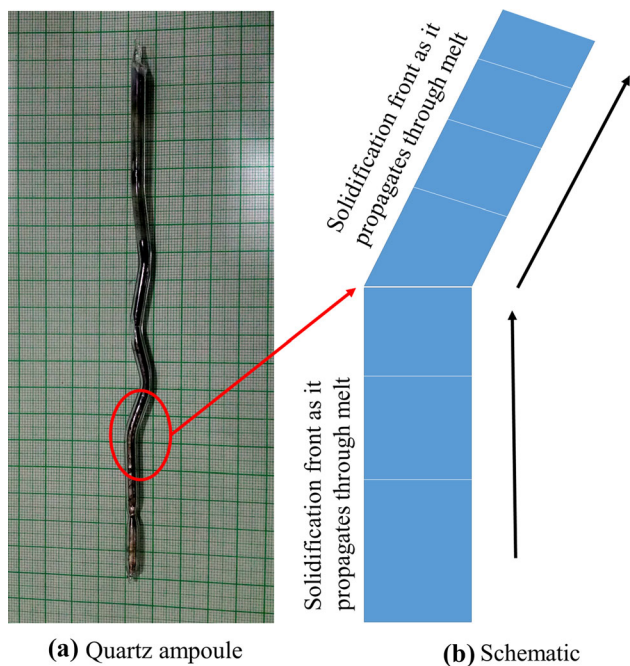
**(a)** Quartz ampoule    **(b)** Schematic

Fig. 13—(*a*) Modified quartz tube showing bends that are intended to cause a change in the orientation of the solid–liquid interface as depicted in (*b*). A small constriction is given at the lower end so as to cause the solidification of a single grain into the straight section of the quartz tube.

has an even lower fraction of Zn-rich phase also exhibits a broken-lamellar morphology with the basal planes of Zn being parallel to the lamellar interface (refer supplementary information file, Figure S7). Apparently then, it is the orientation of the Zn crystal that determines the orientation of the solid–solid interface in these alloys.

In the EBSD results of all our experiments, we do not observe a preferential growth direction to suggest the presence of any interfacial energy anisotropy of the solid–liquid interface. What we do expect, however, is that since the basal plane of Zn is always parallel to the lamellar interface and because of which it seems that Zn decides the orientation of the solid–solid interface, it is likely that the solid–solid interfacial energy is anisotropic, where the orientation for which the lamellar interface becomes parallel to the Zn basal planes, also corresponds to a low-energy direction in the $\gamma$-plot of the solid–solid interfacial energy. In the following, we present experimental evidence of anisotropy in the solid–solid interfacial energy.

## C. *Evidence of Anisotropy*

Experimental evidence of anisotropy may be derived by imposing changes in the growth directions and seeing the relative change in the solid–solid interface orientations. One of the ways of causing a change in the growth direction is by modification of the thermal and solutal gradients in the crucible so as to have biased growth in specific directions. Some of the ways of achieving this is by changing the geometry of the crucible, such as introducing hoops or bends.[40,71]

In the following, we choose a geometry (see Figure 13) of the crucible (quartz tube) that would lead to the introduction of lateral thermal and solutal gradients in the crucible that is intended to influence a change in the growth direction of the crystals. This is because, as the crystals approach a bend, the liquid that is closer to the acute end (the edge of the quartz tube that makes an acute inner angle with the horizontal) of the bend will get hotter with respect to the obtuse end (the edge of the quartz tube that makes an obtuse angle with the inner horizontal) of the quartz tube because of geometric confinement of the released latent heat. This will introduce a lateral thermal gradient over and above the thermal gradient that is imposed in the growth direction leading to a change in the orientation of the resultant thermal gradient. Similarly, the solutal gradients will also get affected as solute rejection in the confined space next to the acute bend compared to the relatively free-liquid ahead of the obtuse bend will lead to a change in the direction of the solutal fluxes. Isotropic crystals would typically be influenced by the change in the thermal and solutal gradients and there would be associated changes in the growth direction of the crystals as shown in Figure 13(b), however, this is not true in the presence of anisotropy. Figure 14 shows a collage of SEM images as the Sn and Zn crystals grow into a quartz bend. We see that the Sn and Zn crystals that are present in the straight section of the quartz tube continue to grow in the same direction, as they grow into the bend, without a change in the orientation of the solid–solid interface. However, at the obtuse end of the quartz tube nucleation of new grains is apparent. We performed a crystallographic analysis at different locations of the longitudinal section of the sample near the bend in order to verify this as highlighted in Figure 15. We find that while the initial eutectic grain continues to grow in the original direction, new Zn crystals continuously nucleate at the obtuse end during growth, whereas the Sn crystal retains its original orientation during growth ahead of the bend. The fact that the original eutectic grain in the straight part of the quartz tube does not change direction, while it moves into the bend, provides apparent evidence that the solid–solid interface is probably corresponding to a low-energy orientation in the $\gamma$-plot of the solid–solid interfacial energy for a given crystallographic relation between the Sn and the Zn crystals. This is the same conclusion that Jaffrey and Chadwick[40] reach on performing a similar experiment. In addition, since we did not determine any fixed growth directions from the crystallography the only reason that remains for noticing such invariance in growth directions with the change in heat and mass flow conditions is possibly because the solid–solid interface is indeed anisotropic.

In order to provide further evidence for the anisotropy in the solid–solid interfacial energy, we performed an additional experiment in which we cut a small piece from a directionally solidified sample and utilize this as a seed for another directional solidification experiment. For the latter experiment, however, we impart a physical rotation to the seed with respect to the original growth direction. This is illustrated in Figure 16 that depicts this

procedure where the original sample is cut at an angle with respect to the growth direction, and then the sample is placed in the quartz tube with the sectioning plane normal perpendicular to the crucible axis. This, therefore, imparts a rotation to the original grain with respect to its previous growth direction. Thereafter, we conduct the directional solidification experiment by utilizing the rotated seed, and the microstructure is depicted in Figure 17(a). Here, we see that the grains upon re-solidification continue to retain the same direction for the solid–solid interface which implies that the growth direction of the crystals is rotated by the same amount as the magnitude of the physical rotation of the seed. We have also verified that the crystals that re-solidify share the same crystallographic orientation of the original seed, as shown, in Figure 17(b) and thus there is no renucleation. Thus, it is clear that once the crystal orientations are fixed, the orientation of the

lamellar interface gets determined and therefore the lamellar orientation in this alloy is a function of the crystallography of the individual phases and not a function of the imposed thermo-solutal conditions as in isotropic crystals. This, therefore, suggests and provides further evidence that the solid–solid interface in the Sn-Zn alloy is anisotropic.

While the crystallographic and experimental characterization indeed points towards the possibility of anisotropy in the solid–solid interfacial energy, we presently do not have an estimation of its form. Additionally, because of the aforementioned reasons, that it is predominantly the Zn crystal that determines the orientation of the solid–solid interface, it seems plausible that the Wulff plot of the solid–solid interface inherits the symmetry of the Zn crystal. A possible approximation with regard the symmetry of the $\gamma$-plot may be derived from the fact that the principal plane
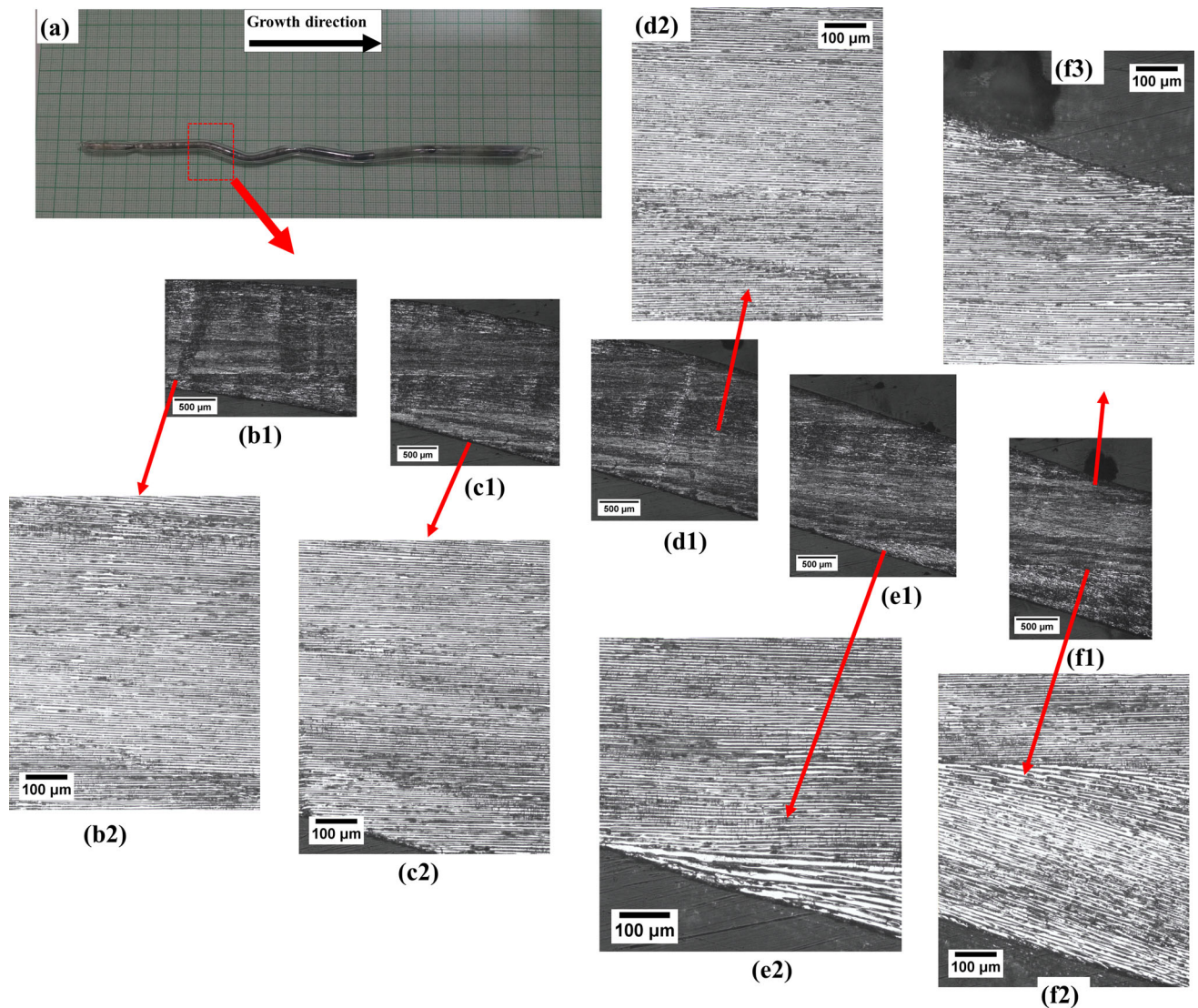


Fig. 14—Collage of SEM images revealing the change in the microstructure as the solidification proceeds across the quartz bend shown in (a), starting from b1 to f1 through c1, d1, e1, respectively, and the corresponding high-magnification images are shown in b2, c2, d2, e2, f2, f3.

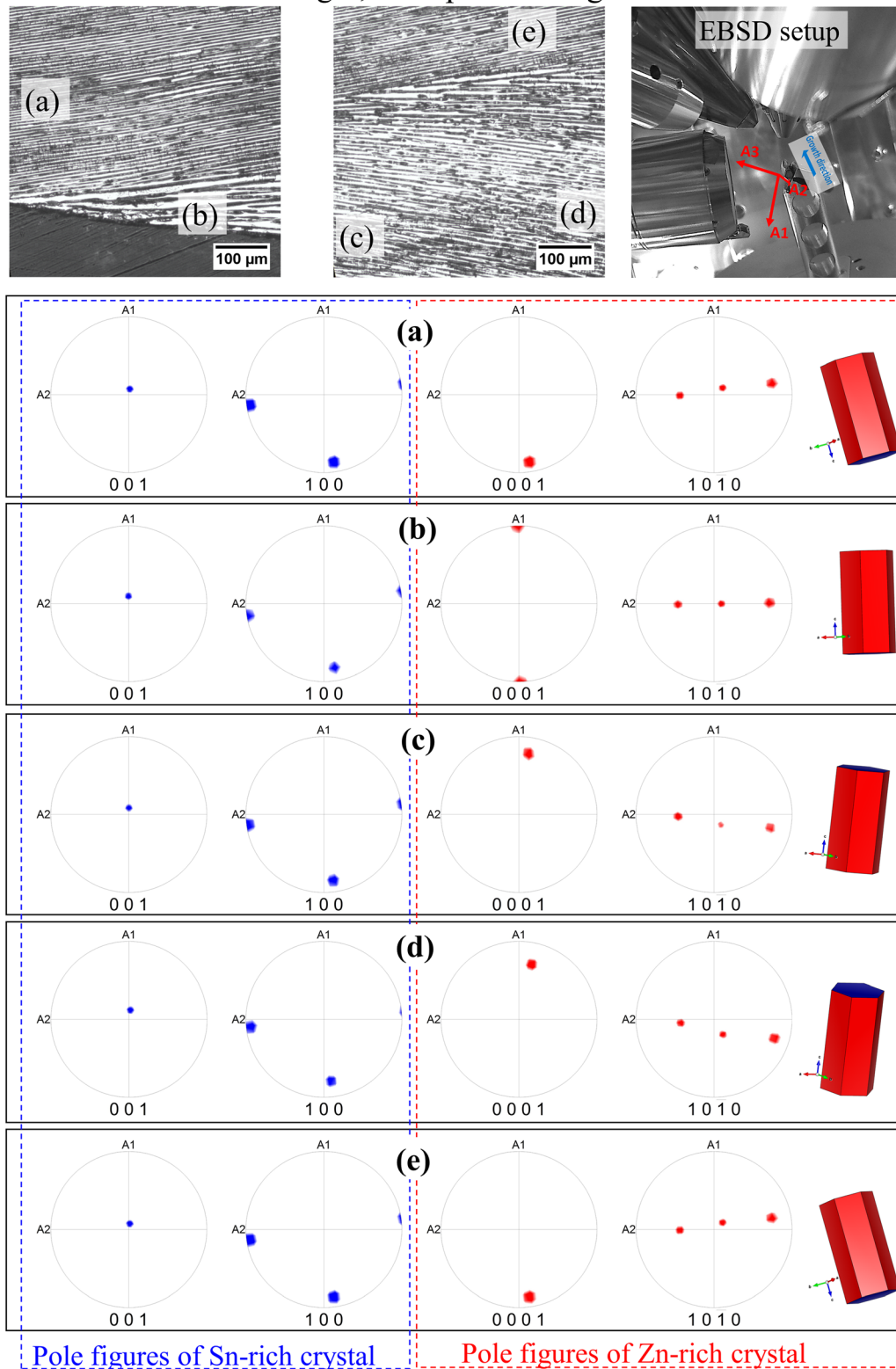For location of the images, refer previous figure



Fig. 15—Crystallographic orientations of the eutectic phases obtained using EBSD at different locations on the longitudinal section (which are highlighted as a, b, c, d, and e on the SEM image) of the sample near the bend in the quartz tube. While Sn maintains its orientation, nucleation of Zn is evident.
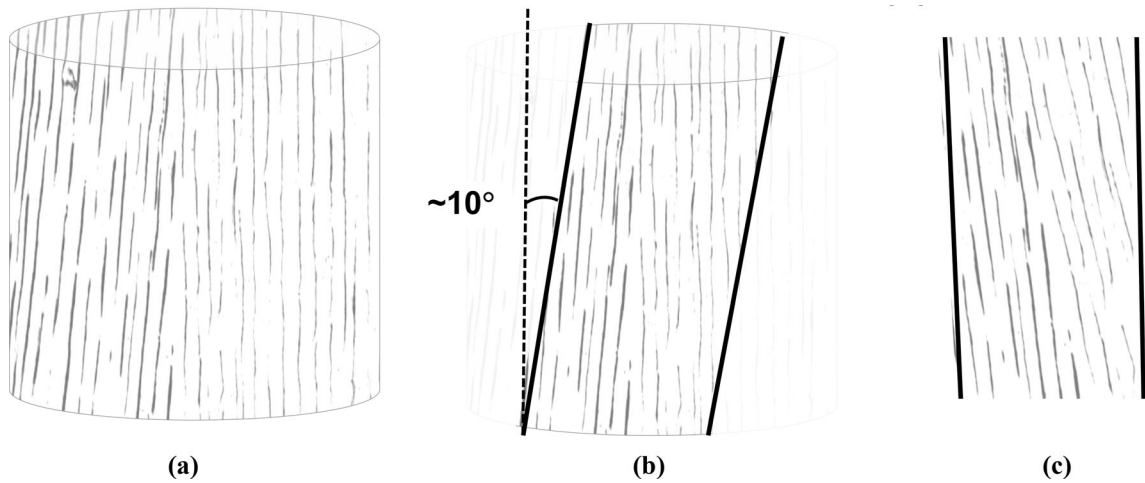
**Fig. 16**—(*a*) Depicts a directionally solidified sample with two grains that is utilized as a seed; one of the grains is aligned straight with respect to the cylindrical axes, while the second has a slight tilt. (*b*) The angle of the cutting plane that dissects the sample at an angle of 10 deg with respect to the growth direction. (*c*) The cut sample is placed such that planes along which the sample is sectioned are aligned with the quartz tube. This, therefore, mimics the situation where the original sample is now rotated with respect to the growth direction.
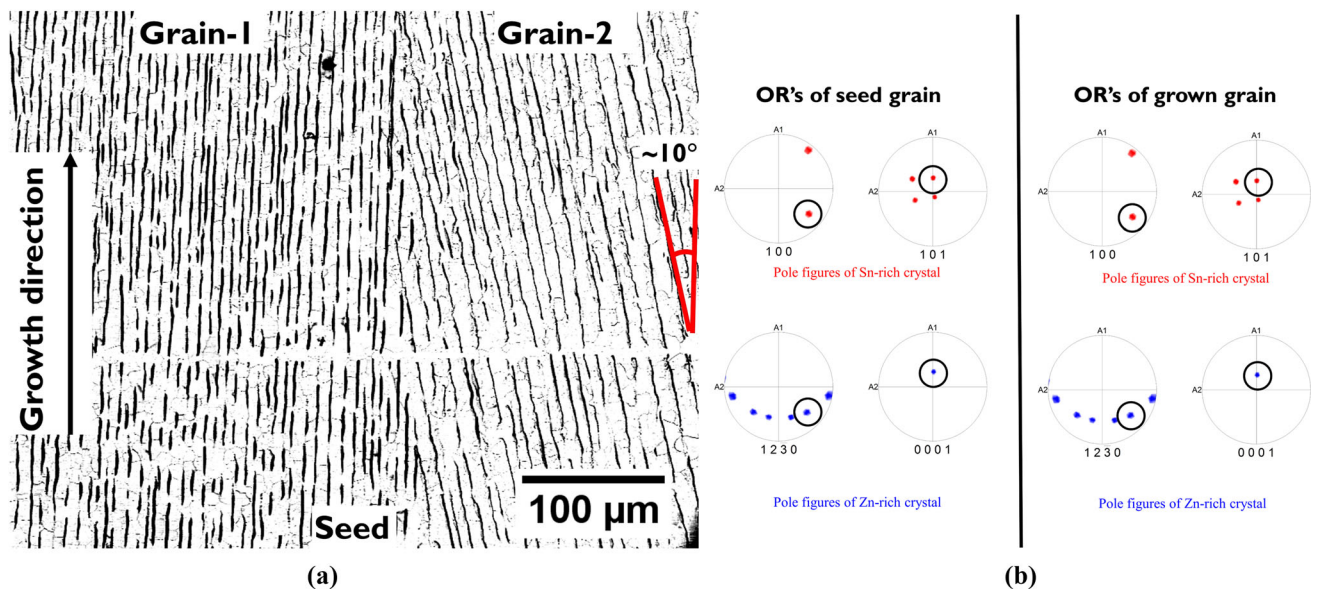


**Fig. 17**—(*a*) Microstructure of the directionally solidified sample that is solidified using a seed. The horizontal discontinuity in the microstructure demarcates the location from which the resolidification begins. (*b*) Pole plots for the Grain-2 in (a) derived from EBSD that show that the crystallographic orientations of resolidified grains match that of the original seed.

that leads to the anisotropy in the solid–solid interfacial energy is the basal plane of the Zn-rich phase. Out-of-plane orientations (perpendicular to the direction of solidification) would then certainly have at least a two-fold symmetry while in-plane rotations (in the plane of the lamellar interface) could have a maximum six-fold symmetry. A quantitative determination of the form and strength of the anisotropy maybe ascertained using RDS[52] that can reveal the trace of solid–solid interface as the orientation of the solid–solid interface is changed during solidification keeping all other parameters fixed. This remains the scope for future work.

However, our proposed hypothesis that the presence of the solid–solid interfacial energy anisotropy leads to the formation of broken-lamellar morphologies forms the motivation of our subsequent paper which presents evidence based on dynamical phase-field simulations.

Finally, while through our results we argue that the solid–solid interface is anisotropic, it is kind of surprising that we do not find evidence for the presence of solid–liquid interfacial energy anisotropy, considering that previous studies[72] show that the Zn–liquid interface is anisotropic particularly because the basal planes of Zn corresponds to a deep minimum in the $\gamma$-plot of

the solid–liquid interfacial energy. We believe this is because the basal plane in the eutectic morphology is parallel to the solid Sn instead of the liquid and thereby we do not observe either faceting of the solid–liquid interface or unique growth directions that would indicate the presence of strong solid–liquid anisotropy. In the configuration, where the basal planes are parallel to the lamellar interface, it is possible that the $\{10\bar{1}0\}$ and $\{11\bar{2}0\}$ face the liquid, and in the microstructures, it is not evident that either of these planes show any faceting. Therefore, while it is true that the presence of solid–liquid interfacial energy anisotropy in an appropriate form could also lead to the formation of lamellar-like structures, however, since we do not find evidence of strong anisotropy in the solid–liquid interfaces, the formation of these structures can most likely be attributed to the presence of anisotropy in the solid–solid interfacial energy.

## IV.  CONCLUSIONS

In this paper, we have investigated two-phase growth in the Sn-Zn alloy, where the minority phase fraction is low. Using directional solidification experiments, we derive that the microstructures during invariant growth in this alloy are predominantly "broken-lamellar." Additionally, from the etched SEM images, we have measured the spacings between the broken-lamellae units and estimated the eutectic scaling constant as $\lambda^2 V$ = 27.04 $\mu$m$^3$/s. We find that the experimental observations of a broken-lamellar arrangement are not in agreement with theoretical predictions based on a Jackson–Hunt type analysis using undercooling vs. spacing relationships of the morphologies. We propose that this deviation is possibly due to the solid–solid interfacial energy being anisotropic that leads to the merger of lamellar fragments along higher interfacial energy orientations. Subsequently, characterization using EBSD of samples obtained from several experiments were conducted, on the basis of which we find two crystallographic relations, i.e., first OR is one of the poles in Sn$\{100\}$ family $\parallel$ Zn$\{0001\}$ and one of the poles in Sn$\{021\}$ family $\parallel$ one of the poles in Zn$\{0\bar{1}10\}$ family; and other OR is one of the poles in Sn$\{101\}$ family $\parallel$ Zn$\{0001\}$ and one of the poles in Sn$\{100\}$ family $\parallel$ one of the poles in Zn$\{21\bar{3}0\}$ family both of which are different from the ones reported in literature. While we do not find a unique orientation relationship, we always find that the basal planes $\{0001\}$ of the Zn-rich phase and either of one of the planes in $\{100\}$ or $\{101\}$ family of the Sn-rich phase are parallel to the solid–solid interfaces that form the lamellar morphology. The fact that the orientation of the Zn crystal always determines the orientation of the lamellar interface points to the possibility that the solid–solid interface is anisotropic. Further, the orientation of the lamellar interface for which it becomes parallel to the basal planes of (Zn) is probably a low-energy orientation in the $\gamma$-plot of the solid–solid interfacial energy. While we do not present the actual Wulff plot of the solid–solid interface, we do show evidence that the solid–solid interface is indeed anisotropic. In a following paper, we elucidate the role of solid–solid interfacial energy anisotropy in the stabilization of lamellar morphologies using dynamical phase-field simulations.

## APPENDIX A. CALCULATION OF THERMAL GRADIENT AT THE SOLID–LIQUID INTERFACE

The model of the directional solidification experimental setup is as shown in Figure A1a. We calculate the thermal profiles by solving heat transfer equations in the software OpenFOAM[65], which allows us to determine accurate thermal gradient at the solid–liquid interface. The material parameters reported by References [43, 64] for the alloy are used in the calculation. The computed thermal profile is shown in Figure A1b. The axial temperature profile (Figure A1c) in liquid shows a gradient close to 6 °C/mm.

## APPENDIX B. CALCULATION OF JACKSON–HUNT PARAMETERS FOR LAMELLAR AND ROD MORPHOLOGY

Using Jackson and Hunt theory,[47] undercooling vs. spacing relation for lamellar (L) and rod morphology (R) writes,

$$\Delta T = K_1 V \lambda + K_2/\lambda. \qquad [B1]$$

For lamellar morphology, $K_1^L = \overline{m} C_o P/f_\alpha f_\beta D$ and $K_2^L = 2\overline{m}(\Gamma_\alpha \sin \theta_\alpha/f_\alpha m_\alpha + \Gamma_\beta \sin \theta_\beta/f_\beta m_\beta)$, where $C_o = (C_\alpha - C_\beta)$ ( i.e., $C_o$ is the composition difference between the solid phases at the eutectic temperature), $f_\alpha$, $f_\beta$ are the volume fractions of the solid phases, $1/\overline{m} = (1/m_\alpha + m_\beta)$, $m_\alpha$, $m_\beta$ are the liquidus slopes of the solid phases. $\Gamma_\alpha$ and $\Gamma_\beta$ are the Gibbs–Thomson coefficients of the solid and the liquid phases while the $\theta_\alpha$ and $\theta_\beta$ are angles the $\alpha$-liquid and the $\beta$-liquid tangents make with the horizontal. $P$ is a function of the volume fraction of one of the phases that reads $\sum_{n=1}^{\infty} \frac{1}{n\pi^3} \sin^2(n\pi f_\alpha)$. Similarly for rod morphology, $K_1^R = \overline{m} C_o M/f_\beta D$, where $M = \sum_{n=1}^{\infty} \frac{1}{(\gamma_n)^3} \frac{J_1^2(\sqrt{f_\alpha}\gamma_n)}{J_0^2(\gamma_n)}$,
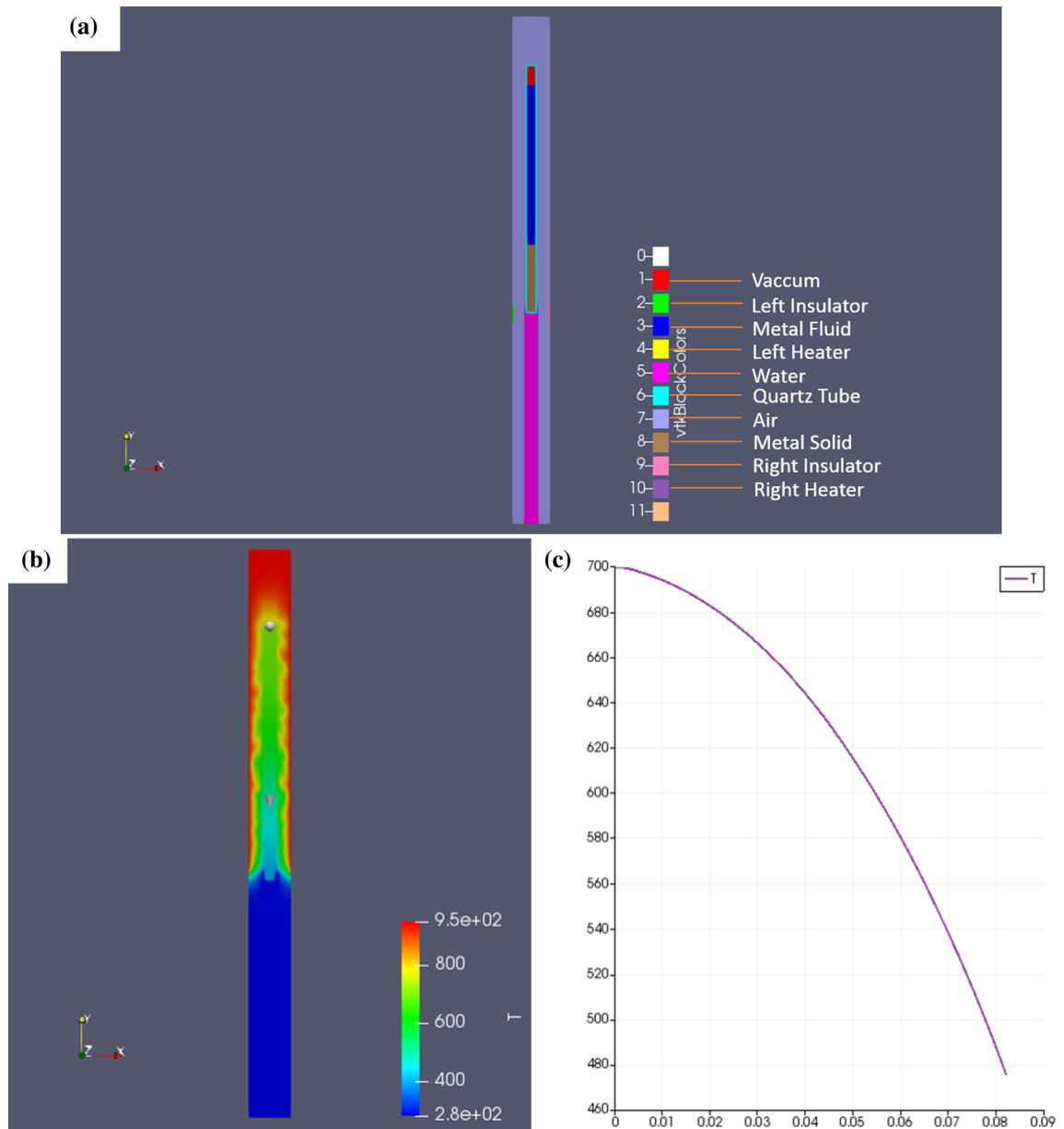
Fig. A1—Modeling using OpenFOAM software, where (*a*) is directional solidification setup 2D view, (*b*) is thermal profile, and (*c*) is axial temperature profile in liquid.

where $\gamma_n$ is the *n*th zero of the first-order Bessel function $J_1$, while $J_o$ is the zeroth-order Bessel function. We calculated $K_1^L$ and $K_1^R$ values as 0.00836 and 0.0018, respectively, using material parameters reported[43,64] for the Sn-Zn alloy. Thereafter using the value of $\lambda^2 V$ ($= K_2^L/K_1^L$) that we find using our experiments, we assessed the value of $K_2^L$ as 0.226. Using the relation $K_2^R/K_2^L = \sqrt{f_\alpha}$ from Jackson–Hunt theory, we calculated $K_2^R$ value as 0.0678. This allows us to determine the $\Delta T$ *vs.* spacing $\lambda$ relationship for both morphologies.

### APPENDIX C. CALCULATION OF INTERFACE SHAPE AND UNDERCOOLING

Assumptions are

- Directional solidification conditions with gradient $G$ and velocity $V$;
- Composition profile derived for a planar solidification interface; and
- All other Fourier coefficients are derived from the planar solution except the boundary layer composition $B_0$

We integrate the basic undercooling equation which writes

$$\Delta T(x) = m^{\nu}(C_E - c(x)) + a/r(x), \qquad [\text{C1}]$$

where $\Delta T$ is the undercooling, $m$ is the liquidus slope of the solid phase concerned, $C_E$ is the eutectic composition, $c(x)$ is the composition profile derived from the solution of the diffusion for a planar solidification front, $a$ is the Gibbs–Thomson coefficient of the relevant solid–liquid interface, while $r(x)$ is its curvature. The composition $c(x)$ can be explicitly written as

$$c(x) = C_E + c_{\infty} + B_0 + \sum_{n=1}^{\infty} B_n \sin\left(\frac{n\pi x}{S_{\alpha} + S_{\beta}}\right), \qquad [\text{C2}]$$

where $B_0$ is the boundary layer composition, $S_{\alpha,\beta}$ are, respectively, the half widths of each of the lamellae. $c_{\infty}$ is the departure of the far-field concentration from the equilibrium value, $C_E$ is the eutectic composition, while each of the Fourier amplitudes $B_n$ can be written as

$$B_n = \frac{2}{(n\pi)^2}\left(S_{\alpha} + S_{\beta}\right)\frac{V}{D} C_0 \sin\left(\frac{n\pi S_{\alpha}}{S_{\alpha} + S_{\beta}}\right), \qquad [\text{C3}]$$

where $C_0$ is $|C_E - C_{\alpha}| + |C_{\beta} - C_E|$ and $D$ is the diffusivity in the liquid.

The undercooling $\Delta T(x)$ can in turn be expressed using the thermal gradient and the interface position as

$$\begin{aligned}\Delta T &= T_E - (T_0 + G(z - z_0)) \\ &= (T_E - (T_0 + Gz_0)) - Gz \qquad [\text{C4}] \\ &= \Delta T_0 - Gz\end{aligned}$$

$T_0$ and $z_0$ being the temperature and z-ordinate of the triple point which is shared by both solid–liquid interfaces. The composite term $(T_E - (T_0 + Gz_0))$ is expressed as $\Delta T_0$ which by definition is the same for both the phases. With this Eqn. C1 becomes,

$$\Delta T_0 - Gz = m^{\nu}(C_E - c(x)) + a/r(x). \qquad [\text{C5}]$$

Integrating the preceding equation once over each of the solid–liquid interfaces, with the boundary conditions, that the center of each of the phases is flat and the tangent at the triple point is given by the balance of the surface tensions, we derive two relations, respectively, for each of the solid–liquid interfaces, which can be written as

$$\Delta T_0 - G\bar{z}^{\alpha} - m^{\alpha}\left(-c_{\infty} - B_0 - 2\frac{\lambda V}{D}C_0 P(\eta_{\alpha})\right)$$
$$= a^{\alpha}\frac{\sin(\theta_{\alpha l})}{\eta_{\alpha}\lambda}$$
$$\Delta T_0 - G\bar{z}^{\beta} - m^{\beta}\left(-c_{\infty} - B_0 + 2\frac{\lambda V}{D}C_0 P(\eta_{\alpha})\right) \qquad [\text{C6}]$$
$$= a^{\beta}\frac{\sin(\theta_{\beta l})}{\eta_{\alpha}\lambda},$$

where $\lambda = S_{\alpha} + S_{\beta}$, and $\eta_{\alpha} = S_{\alpha}/(S_{\alpha} + S_{\beta})$, while $\bar{z}^{\alpha}$ and $\bar{z}^{\beta}$ are average interface positions of the $\alpha$ and the $\beta$ interfaces, respectively. $P(\eta_{\alpha})$ is written as $\sum_{n=1}^{\infty}\frac{\sin^2(n\pi\eta_{\alpha})}{(n\pi)^3}$

The previous expressions can now be simplified to derive $\Delta T_0$ as well as $B_0$ in terms of the average interface positions as

$$\begin{aligned}B_0 &= G\frac{(\bar{z}^{\alpha} - \bar{z}^{\beta})}{m^{\beta} - m^{\alpha}} \\ &+ \frac{1}{m^{\beta} - m^{\alpha}}\left(\frac{a^{\alpha}\sin(\theta_{\alpha l})}{\eta_{\alpha}\lambda} - \frac{a^{\beta}\sin(\theta_{\beta l})}{(1 - \eta_{\alpha})\lambda}\right) \qquad [\text{C7}] \\ &- \frac{2\lambda V C_0 P}{D(m^{\beta} - m^{\alpha})}\left(\frac{m^{\alpha}}{\eta_{\alpha}} - \frac{m^{\beta}}{1 - \eta_{\alpha}}\right),\end{aligned}$$

while $\Delta T_0$ is written as

$$\begin{aligned}\Delta T_0 &= G\bar{z}^{\alpha} + m^{\alpha}\left(-c_{\infty} - B_0 - \frac{2\lambda V C_0 P}{D\eta_{\alpha}}\right) \\ &+ \frac{a^{\alpha}\sin(\theta_{\alpha l})}{\eta_{\alpha}\lambda}\end{aligned} \qquad [\text{C8}]$$

Thereafter we set out to integrate Eqn. C5 using a finite difference approach where we discretize the curvature using central differences and the slopes as one-sided forward differences. The boundary conditions again involve imposing a zero slope at the mid-points of the lamellae which are at $x = 0$ and $x = S_{\alpha} + S_{\beta}$. Also, the tangents at the triple point $x = S_{\alpha}$ are given by the Young's condition. In this discretized equation, the derived expressions for $B_0$ and $\Delta T_0$ which are expressed in Eqns. C7 and C8 are used. This gives us a set of N-2 non-linear equations (N being the points on a particular solid–liquid interface) for each of the solid–liquid interfaces, which are solved using the non-linear solution routine of "fsolve" which is in the optimization tool box of "octave-forge." The result is the solution to the interface z-ordinates of each of the solid–liquid interface from which one can derive both the boundary layer composition $B_0$ and $\Delta T_0$ and thereby the temperature of the triple point $T_0$ (since $z_0$ is derived from the solution) along with the temperatures along each of the solid–liquid interface.

## ELECTRONIC SUPPLEMENTARY MATERIAL

## REFERENCES

1. W. Kurz, D.J. Fisher: *Fundamentals of Solidification*, vol. 1: trans tech publications Aedermannsdorf, Switzerland, 1986.

2. J.A. Dantzig, M. Rappaz, *Solidification*, EPFL Press, 2009.
3. G.A. Chadwick: *Prog. Mater. Sci.*, 1963, vol. 12, pp. 99–182.
4. J. Hunt and K. Jackson: *Trans. Metall. Soc. AIME*, 1966, vol. 236 (6), pp. 843–52.
5. R. Elliott: *Eutectic Solidification Processing: Crystalline and Glassy Alloys*, Elsevier, 2013.
6. M. Croker, R. Fidler, and R. Smith: *Proc. R. Soc. Lond. A*, 1973, vol. 335 (1600), pp. 15–37.
7. K. Kassner and C. Misbah: *Phys. Rev. A*, 1991, vol. 44 (10), p. 6513.
8. U. Hecht, L. Gránásy, T. Pusztai, B. Böttger, M. Apel, V. Witusiewicz, L. Ratke, J. De Wilde, L. Froyen, D. Camel, B. Drevet, G. Faivre, S.G. Fries, B. Legendre, and S. Rex: *Mater. Sci. Eng.*, 2004, vol. 46 (1–2), pp. 1–49.
9. A. Karma and M. Plapp: *JOM*, 2004, vol. 56 (4), pp. 28–32.
10. H. Walker, S. Liu, J. Lee, and R. Trivedi: *Metall. Mater. Trans. A*, 2007, vol. 38A, pp. 1417–25.
11. A. Parisi and M. Plapp: *Acta Mater.*, 2008, vol. 56 (6), pp. 1348–57.
12. M. Perrut, S. Akamatsu, S. Bottin-Rousseau, and G. Faivre: *Phys. Rev. E*, 2009, vol. 79 (3), p. 032602.
13. M. Asta, C. Beckermann, A. Karma, W. Kurz, R. Napolitano, M. Plapp, G. Purdy, M. Rappaz, and R. Trivedi: *Acta Mater.*, 2009, vol. 57 (4), pp. 941–71.
14. S. Akamatsu and M. Plapp: *Curr. Opin. Solid State Mater. Sci.*, 2016, vol. 20 (1), pp. 46–54.
15. R. Contieri, C. Rios, M. Zanotello, and R. Caram: *Mater. Charac.*, 2008, vol. 59 (6), pp. 693–99.
16. A. Dennstedt and L. Ratke: *Trans. Indian Inst. Metals*, 2012, vol. 65 (6), pp. 777–82.
17. A. Choudhury: *Trans. Indian Inst. Metals*, 2015, vol. 68 (6), pp. 1137–43.
18. J. Hötzer, M. Jainta, P. Steinmetz, B. Nestler, A. Dennstedt, A. Genau, M. Bauer, H. Köstler, and U. Rüde: *Acta Mater.*, 2015, vol. 93, pp. 194–204.
19. J. Hötzer, P. Steinmetz, M. Jainta, S. Schulz, M. Kellner, B. Nestler, A. Genau, A. Dennstedt, M. Bauer, H. Köstler, and U. Rüde: *Acta Mater.*, 2016, vol. 106, pp. 249–59.
20. P. Steinmetz, J. Hötzer, M. Kellner, A. Dennstedt, and B. Nestler: *Comput. Mater. Sci.*, 2016, vol. 117, pp. 205–14.
21. S. Liu, J. Lee, and R. Trivedi: *Acta Mater.*, 2011, vol. 59 (8), pp. 3102–15.
22. D. Cooksey, D. Munson, M. Wilkinson, and A. Hellawell: *Phil. Mag.*, 1964, vol. 10 (107), pp. 745–69.
23. A. Parisi and M. Plapp: *EPL (Europhysics Letters)*, 2010, vol. 90 (2), p. 26010.
24. D. Lewis, J. Warren, W. Boettinger, T. Pusztai, and L. Gránásy: *JOM*, 2004, vol. 56 (4), pp. 34–39.
25. M. Taylor, R. Fidler, and R. Smith: *J. Cryst. Growth*, 1968, vol. 3, pp. 666–73.
26. T. Digges and R. Tauber: *Metall. Trans.*, 1971, vol. 2 (6), pp. 1683–89.
27. H. Kerr and M. Lewis: *J. Cryst. Growth*, 1972, vol. 15 (2), pp. 117–25.
28. T. Digges, Jr and R. Tauber: *J. Cryst. Growth*, 1971, vol. 8 (1), pp. 132–34.
29. M. Savas, L. Clapham, and R. Smith: *J. Mater. Sci.*, 1990, vol. 25 (2), pp. 909–13.
30. H. Kerr and W. Winegard: *Can. Metall. Q.*, 1967, vol. 6 (1), pp. 67–70.
31. M. Taylor, R. Fidler, and R. Smith: *Metall. Trans.*, 1971, vol. 2 (7), pp. 1793–98.
32. M. Şahin and E. Çadirli: *J. Mater. Sci.*, 2012, vol. 23 (2), pp. 484–92.
33. J. Bromley, F. Vnuk, and R. Smith: *J. Mater. Sci.*, 1983, vol. 18 (10), pp. 3143–53.
34. G Piatti and G. Pellegrini: *J. ScieMaterialsnce*, 1976, vol. 11 (5), pp. 913–24.
35. G. Beghi, G. Piatti, and K. Street: *J. Mater. Sci.*, 1971, vol. 6 (2), pp. 118–25.
36. M. Notis, D. Shah, S. Young, and C. Graham: *IEEE Trans. Magn.*, 1979, vol. 15 (2), pp. 957–66.
37. M. Sahoo, G. Delamore, and R. Smith: *J. Mater. Sci.*, 1980, vol. 15 (5), pp. 1097–1103.
38. G. Nishimura, R. Fidler, M. Taylor, and R. Smith: *Can. Metall. Q.*, 1969, vol. 8 (4), pp. 319–22.
39. P. Taylor, H. Kerr, and W. Winegard: *Can. Metall. Q.*, 1964, vol. 3 (3), pp. 235–37.
40. D. Jaffrey and G. Chadwick: *Metall. Trans.*, 1970, vol. 1 (12), pp. 3389–96.
41. F. Vnuk, M. Sahoo, D. Baragar, and R. Smith: *J. Mater. Sci.*, 1980, vol. 15 (10), pp. 2573–83.
42. H. Kaya, M. Gündüz, E. Çadirli, and O. Uzun: *J. Mater. Sci.*, 2004, vol. 39 (21), pp. 6571–76.
43. H. Kaya, E. Çadrlı, and M. Gündüz: *J. Mater. Eng. Perform.*, 2003, vol. 12 (4), pp. 456–69.
44. Y. Goto, M. Kurosaki, and H. Esaka: *J. Jpn. Inst. Metals*, 2011, vol. 75 (7), pp. 392–97.
45. M. Şahin and F. Karakurt: *Phys. B*, 2018, vol. 545, pp. 48–54.
46. K. Sharma and R. Rai: *Thermochim. Acta*, 2012, vol. 535, pp. 66–70.
47. K.A. Jackson and J.D. Hunt: *Trans. Metall. Soc. AIME*, 1966, vol. 236, pp. 1129–42.
48. B. Caroli, C. Caroli, G. Faivre, and J. Mergy: *J. Cryst. Growth*, vol. 118 (1992).
49. A. Valance, C. Misbah, D. Temkin, and K. Kassner: *Phys. Rev. E* vol. 48, (1993).
50. S. Bottin-Rousseau, M. Şerefoğlu, S. Akamatsu, and G. Faivre: *IOP Conference Series: Materials Science and Engineering*, vol. 27 (1), pp. 012088, (2012).
51. S. Akamatsu, S. Bottin-Rousseau, M. Şerefoğlu, and G. Faivre: *Acta Mater.*, 2012, vol. 60 (6–7), pp. 3199–3205.
52. S. Akamatsu, S. Bottin-Rousseau, M. Şerefoğlu, and G. Faivre: *Acta Mater.*, 2012, vol. 60 (6–7), pp. 3206–14.
53. S. Ghosh, A. Choudhury, M. Plapp, S. Bottin-Rousseau, G. Faivre, and S. Akamatsu: *Phys. Rev. E*, 2015, vol. 91 (2), p. 022407.
54. S. Ghosh and M. Plapp: *Acta Mater.*, 2017, vol. 140, pp. 140–48.
55. U. Hecht, J. Eiken, S. Akamatsu, and S. Bottin-Rousseau: *Acta Mater.*, 2019, vol. 170, pp. 268–77.
56. S. Bottin-Rousseau, O. Senninger, G. Faivre, and S. Akamatsu: *Acta Mater.*, 2018, vol. 150, pp. 16–24.
57. S. Mohagheghi, U. Hecht, S. Bottin-Rousseau, S. Akamatsu, G. Faivre, and M. Şerefoğlu: Effects of interphase boundary anisotropy on the three-phase growth dynamics in the β (in)–in2bi–γ (sn) ternary-eutectic system: In: IOP Conference Series: Materials Science and Engineering: Vol. 529: IOP Publishing, p. 012010, (2019).
58. R. Elliot and A. Moore: *Scripta Metall.*, 1969, vol. 3 (4), pp. 249–51.
59. P. Pandey, C. Tiwary, and K. Chattopadhyay: *J. Electr. Mater.*, 2016, vol. 45 (10), pp. 5468–77.
60. P. Pandey, C. Tiwary, and K. Chattopadhyay: *J. Electr. Mater.*, 2019, vol. 48 (5), pp. 2660–69.
61. M. Straumanis and N. Brakes: *Z. Physik. Chem. B*, vol. 38 (1937).
62. H. Herman: *Adv. Mater. Res.* Vol. 4: Wiley-Interscience (1970).
63. B. Cantor and G. Chadwick: *J. Cryst. Growth*, 1975, vol. 30 (1), pp. 109–112.
64. Z. Moser, J. Dutkiewicz, W. Gasior, and J. Salawa: *J. Phase Equil.*, 1985, vol. 6 (4), pp. 330–34.
65. H.G. Weller, G. Tabor, H. Jasak, and C. Fureby: *Comput. Phys.*, 1998, vol. 12 (6), pp. 620–31.
66. A.J. Shahani, X. Xiao, and P.W. Voorhees: *Nat. Commun.*, 2016, vol. 7, p. 12953.
67. I. Ansara, A.T. Dinsdale, and M.H. Rand: *COST 507, Thermochemical Database for Light Metal Alloys*, vol. 2, Office for Official Publication of the European Communities, Luxemburg, 1998.
68. A.J. Schwartz, M. Kumar, B.L. Adams, and D.P. Field: *Electron Backscatter Diffraction in Materials Science*, Springer, 2000.
69. D.B. Williams and C.B. Carter: *The Transmission Electron Microscope*, Springer, 1996.
70. D.P. Field: *Ultramicroscopy*, 1997, vol. 67 (1–4), pp. 1–9.
71. L.G. Ware, D.H. Suzuki, and Z.C. Cordero: *J. Mater. Sci.*, 2020, vol. 55, pp. 1–12.
72. A. Passerone and N. Eustathopoulos: *Acta Metall.*, 1982, vol. 30 (7), pp. 1349–56.